Optimizing the p-contact of nip substrate solar cell

for multi-junction device

Ashish Binani
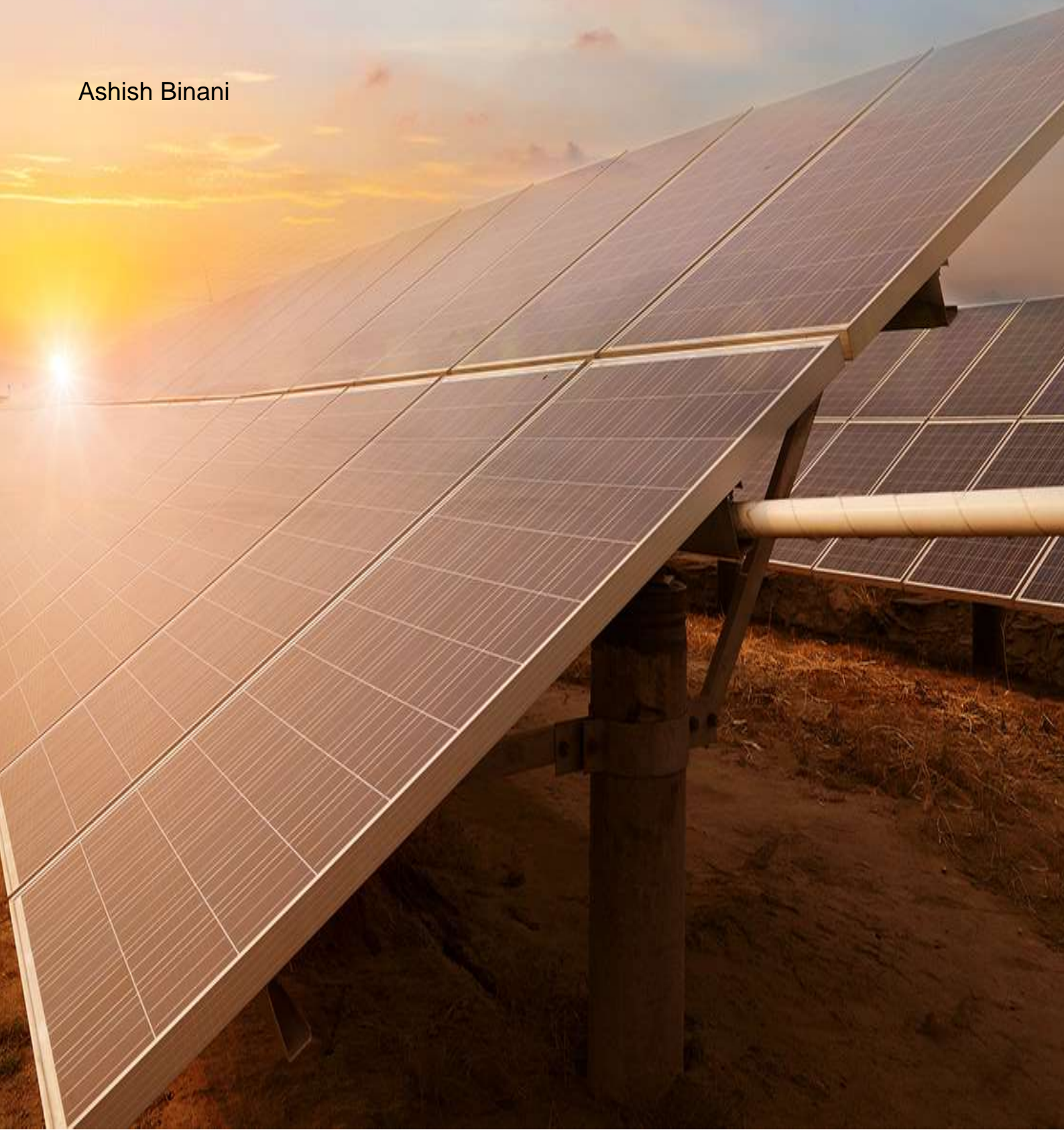
Optimizing the p-contact of nip substrate Solar cell

For multi-junction device

By

Ashish Binani

in partial fulfilment of the requirements for the degree of

Master of Science

in Electrical Power Engineering

at the Delft University of Technology,
to be defended publicly on Friday November 29, 2019 at 10:00 AM.

Student number:	4738950	
Thesis committee:	Prof. dr. ir. A.H.M. Smets	TU Delft, Supervisor
	Dr. R.A.C.M.M. van Swaaij	TU Delft, Associate Professor
	Dr. Milos Cvetkovic	TU Delft, Assisstant Professor
	Ir. T. de Vrijer	TU Delft, Daily supervisor

This thesis is confidential and cannot be made public until November 29, 2019.

An electronic version of this thesis is available at http://repository.tudelft.nl/.

ॐ भूर् भुवः सुवः ।
तत्सवितुर्वरेण्यं
भर्गो देवस्यधीमहि ।
धियो यो नः प्रचोदयात् ॥

"We meditate on the all prevailing brightness and brilliance of the God, The Sun. May he propel our intellects"

Acknowledgement

The journey of my masters course has come to a beautiful ending. With new experiences and knowledge, I feel more confident to face the future in sustainable energy industry. I would like to present my sincere admiration and gratitude to Professor Arno Smets for guiding me in my masters thesis. His cheerfulness and positivity have inspired and encouraged millions of students like me to learn about the basics of solar energy.

I would also like to express my regards to my daily supervisor, Thierry de Vrijer. He has been one of the most prompt person to help me whenever needed. The calmness with which he explains the concepts and demonstrates the use of equipment was unparallel. His commitment and vast expanse of knowledge has been a huge help throughout the journey.

My sincere thanks to Dr. Rene van Swaaij and Dr. Milos Cvetkovic for sparing their time to participate in my masters thesis committee.

My friends have been my support through my ups and down. Specially Steven Roerink, with whom I shared my first clean room experiences and the problems during depositions.

All of these had not been possible if it wasn't for the support, love and care of my family. I will try my best to make you all proud.

Ashish Binani

Delft, November 2019.

Abstract

Single junction solar cells have a theoretical efficiency limit of 33.1% due to spectral mismatch. To overcome this limitation, two or more single junction cells with different bandgaps can be coupled together to achieve higher energy conversion efficiency by optimum spectral utilization. In this work, thin film silicon-based alloys are used to obtain a high potential and a current matched 2-junction solar cell is fabricated. The top cell is a-Si which has high bandgap of 1.8eV and the bottom cell is a-SiGe:H which has a tuneable bandgap between 1.4-1.6eV.

This thesis will focus in optimizing the window layer of the top a-Si solar cell and the effects of Hydrogen Plasma Treatment (HPT) at the i/p and p/TCO interface. This top cell is fabricated in a PECVD cluster tool in *n-i-p* substrate configuration on ASAHI glass substrate. The use of PECVD allows for a better control of the layer properties by changing the gas flow rates and the deposition environment.

Initially a reference cell is fabricated which had an open circuit voltage (V_{oc}) of 804 mV, a fill factor (FF) of 0.63, a short circuit current density (J_{sc}) of 12.8 mAcm-2 and an efficiency of 6.56 %. To improve the performance of the solar cell the the effects of HPT on the material properties of the i-layer and the p-layer are studied at varying power, pressure and duration of exposure. The next step is to study the effects of the precursor gas flow rates for the deposition of p-nc-SiO$_x$ layer and optimize the thickness of the individual components of the window layer including the TCO.

The optimization process involved trading off certain properties in favour of a high Voc and high FF. The final cell had an open circuit voltage (V_{oc}) of 863V, a fill factor (FF) of 0.655, a short circuit current density (J_{sc}) of 12.5 mAcm-2 and an efficiency of 7.06 %. Thus, by only optimizing the non-active window layer an open circuit voltage gain of 60mV is achieved with an improved FF.

This single junction cell is then fabricated on top of a-SiGe:H solar cell. With some iteration in the absorber layer properties of both the top and bottom cells, the final tandem cell had a V_{oc} of 1395 mV, a FF of 0.69, the current limiting J_{sc} of the top cell at 8.34mAcm^{-2} and an overall efficiency of 7.99%. To further improve this tandem cell, the tunnel recombination junction can be further optimised.

Contents

List of Figures

List of Tables

Nomenclature

Abbreviations

CO_2	Carbon Dioxide
UN	United Nations
AM	Air Mass
IEC	International Electrotechnical Commission
EM	Electromagnetic
HPT	Hydrogen Plasma Treatment
PV	Photovoltaic
SQ	Shockley-Queisser
SRH	Shockley-Read-Hall(recombination)
c-Si	Crystalline Silicon
a-Si	Amorphous Silicon
SiGe	Silicon Germanium
:H	Hydrogenated
TFSSC	Thin Film Silicon Solar Cell
PECVD	Plasma Enhanced Chemical Vapour Deposition
EQE	External Quantum Efficiency
TCO	Transparent Conducting Oxide
ITO	Indium Tin Oxide
FTO	Fluorine-doped Tin Oxide
AZO	Aluminium-doped Zinc oxide

Latin Letters

D	Diffusion Coefficient
E	Energy
FF	Fill Factor
f	Fermi-Dirac distribution
G	Generation rate
g	Density of state function
I	Current
I_e	Irradiance
J	Current density
n	Electron concentration
n	Refractive index (real part)
p	Hole concentration
P	Power
R	Recombination rate
R	Reflectivity
T	Temperature

T	Transmittance
V	Electric Potential

Greek Letters

α	Absorption coefficient
ε	Electric permittivity
ε	Emissivity
η	Efficiency
κ	Refractive index (imaginary part)
λ	Wavelength
μ	Mobility
ν	Frequency
ρ	Charge density
σ	Conductivity
τ	Lifetime
φ	Work function

Subscripts

C	Conduction Band
D	Donor
d	Drift
F	Fermi
G	Bandgap
i	Intrinsic, incident
oc	open-circuit
ph	Photon
r	Reflected
sc	short-circuit
t	Transmitted
th	Thermal
V	Valance Band

Constants

c_0	Speed of light in vacuum (299792458 ms^{-1})
ε_0	Vacuum permittivity (8.854×10^{-12} AsV^{-1}m^{-1})
F	Faraday constant ()
h	Plank's constant ()
k_B	Boltzmann constant ()
μ_0	Vacuum permeability ()
q	Elementary charge (1.602×10^{-9} C)

1. Introduction

1.1 Introduction

Quality of life is related to the magnitude of energy consumption devices in daily use. After the industrial revolution there has been exponential growth in the demand and supply of energy as can be seen in figure 1[1]. The most abundant, and relatively easy to procure, form of energy was fossil fuels like coal, oil and natural gas. The use of fossil fuels resulted in emission of various greenhouse gasses like carbon˙dioxide (CO_2), which in-turn is raising the global average temperature. The ill-effects of fossil fuel as primary energy source were unnoticed in the initial stages but has become clearer since the start of the 21st century (figure 2 [2]). The pursuit to limit the rise in temperature well below 2°C was laid down at the UN Climate Change Conference in Paris in 2015.
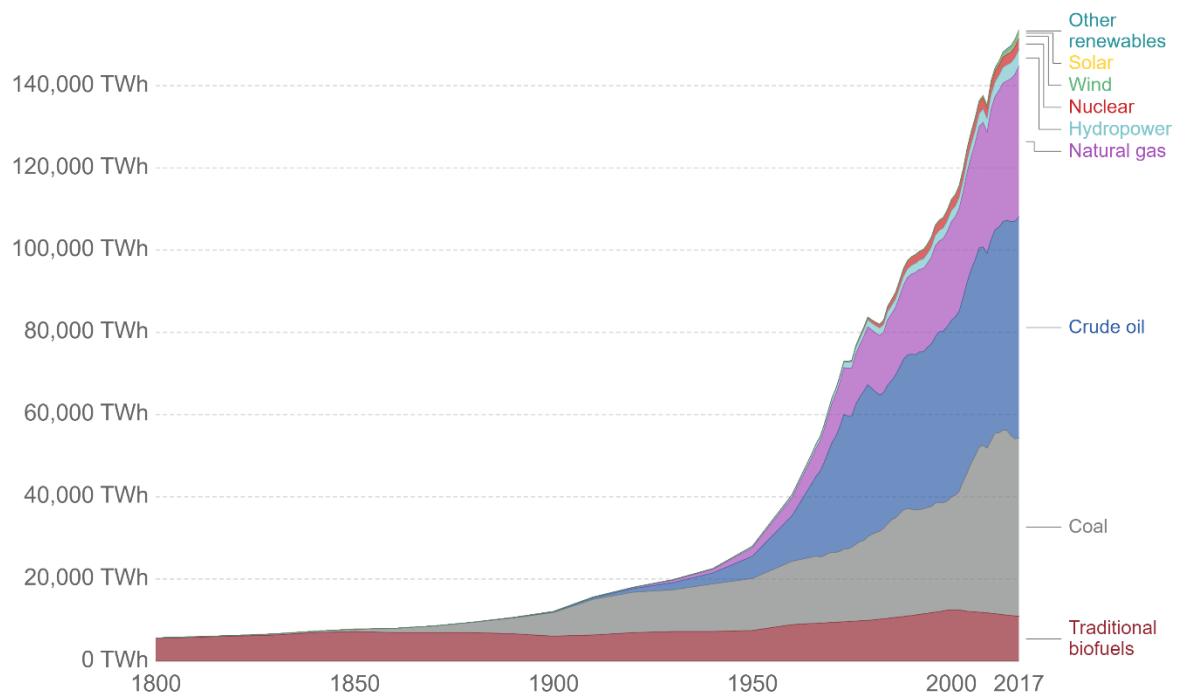
Figure 1: Global Primary Energy Consumption.

The limited supply of oil/natural gas has also been one of the major factors controlling the economy of the world. The implementation and use of renewable energy sources in the existing grid attempt to limit global warming but also can act as a cost-effective alternative to petroleum-based sources. Wind, hydro and solar energy form a triad of clean and unlimited sources of energy albeit without a continuous supply. This creates a mismatch in production and consumption times. This mismatch can be overcome with the use of various energy storage devices like Lithium batteries, green hydrogen, and other forms of chemical fuel manufactured with the excess renewable energy. The battery technology is expensive and cannot be used for
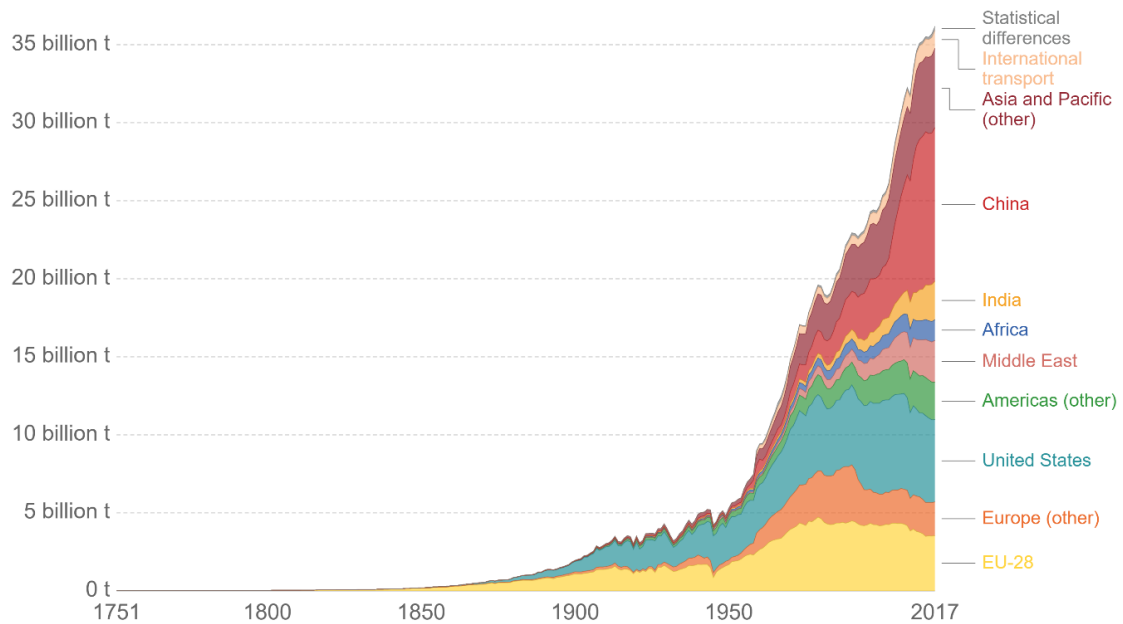
Figure 2: Global CO₂ emissions.

long term storage. Solar energy can be used to generate green hydrogen by splitting water molecules. This hydrogen can be used as is or be converted to chemical fuels like methane or formic acid by reaction with carbon dioxide. These chemical reactions require a specific potential difference to work. To achieve the required voltage and increase the spectral utilization of the incident solar radiation, multi-junction solar cells can be implemented in the photoelectrochemical devices. In this thesis, optimization of the top layers/window layer of one such multijunction solar cell is discussed.

1.2 Fundamentals of Solar Cells

The spectral distribution of the Sun's energy over a range of wavelength helps in characterising the performance of a solar cell. This energy, also called irradiance, is visualised in figure 3[3].
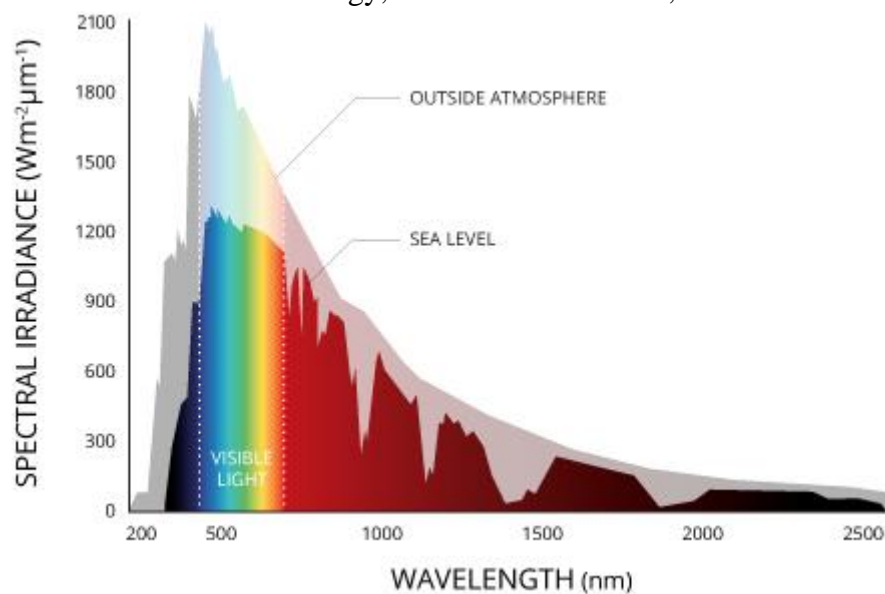
Figure 3: Solar Spectrum

2

The spectrum AM0 (air mass zero) is the irradiance measured just outside the earth's atmosphere while AM1.5 is the standardised Solar spectral irradiance, as in International Standard IEC 60904-3[4], at sea level. The irradiance at AM1.5 is calculated using the formula:

$$I_e = \int \frac{hc}{\lambda} \Phi(\lambda) d\lambda = 1000\text{W/m}^2 \tag{1.1}$$

Where, I is Irradiance,
$\Phi(\lambda)$ is spectral photon flux at wavelength λ.

A solar cell works on the principle of the Photovoltaic (PV) effect, as it develops a voltage/potential difference between two dissimilar materials when exposed to Electromagnetic (EM) radiations. With a high surface temperature of about 6000K, the sun acts as a blackbody and emits EM radiation. These EM waves consist of energy packets called photons whose magnitude is expressed according to the formula:

$$E = \frac{hc}{\lambda} \tag{1.2}$$

Where, h is the Plank's constant,
c is the speed of light (EM wave),
λ is the wavelength of the light (EM wave).

The effect of EM radiation in materials can be explained in detail based on the atomic structure of the materials which can be described by the energy band diagram figure 4[5]. This effect is known as photoelectric effect which was postulated by Albert Einstein.
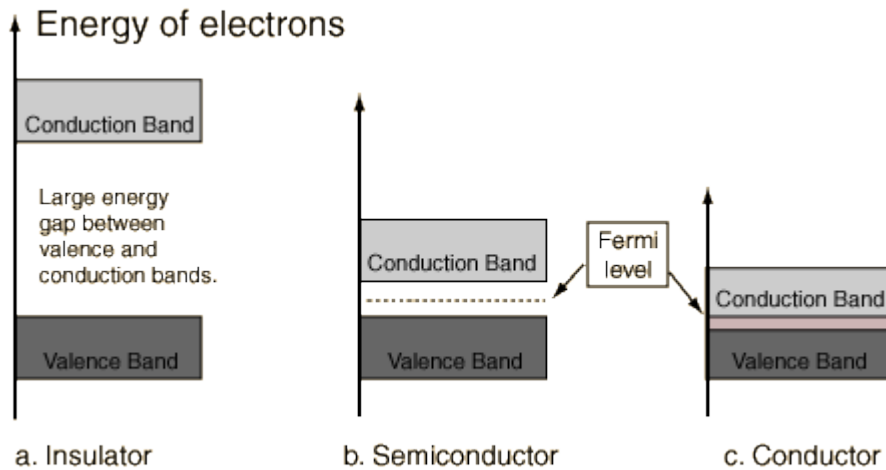
Figure 4: Energy Band Diagrams.

The incident light imparts its energy to the electrons in the material which rises to a higher atomic level corresponding to the final energy of the electron. If the energy is higher than the threshold, the electron may jump from valence bands to conduction band. The Energy gap between the valance band and conduction band is known as Bandgap Energy (E_G) of the material. In metals valence and conduction bands overlap thus allowing the electrons to move freely making them always conductive. The energy gap between the valance band and

3

conduction band of insulators is too large to be overcome by the energy of the incident light from our sun. Semiconductor materials have a small bandgap energy which is essential for the PV effect.

The PV effect in a solar cell can be simplified in 4 steps:

1. Absorption of Light
2. Generation of excess electrically charged carriers
3. Separation of the positive and negative charge carriers
4. Collection of the positive and negative charge carriers in external circuit

Ideal absorption of light occurs when the energy of the incident photon is equal to the bandgap energy. There are two other possibilities when the photon energy (E_{ph}) is less or more than the bandgap. These account for the two primary losses in a single junction solar cell, namely non-absorption and thermalization, as visualised in figure 5.
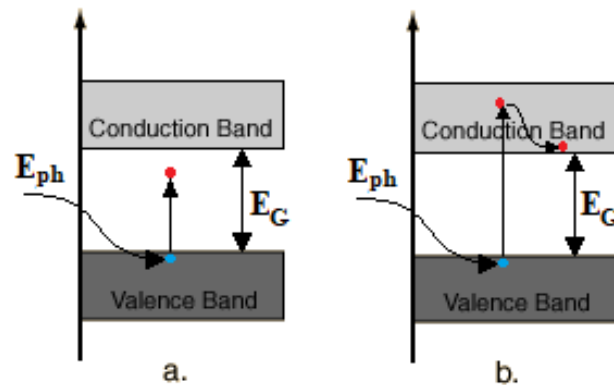
Figure 5: a.) Non-absorption; b.) Thermalization.

In non-absorption, the E_{ph} is less, than E_G, to generate electron hole free charge carriers. Photons with energy greater than the bandgap excite the electrons to a much higher level resulting in release of energy in the form of heat to attain the lower conduction state.

Along with the spectral mismatch, there are some electrical losses which limit the performance of a solar cell. The theoretical efficiency limit for a single junction solar cell is given by the Shockley-Queisser (SQ) limit [6]. The figure 6 shows the components of for a semiconductor material with bandgap energy of 1.34eV at AM1.5 spectrum, this limit is 33.1% [7].

For an intrinsic semiconductor, the concentration of free electrons and holes are equal in thermal equilibrium. For doped semiconductor materials, the excess free charge carriers are the majority charge carriers, i.e., electrons for n-doped and holes for p-doped.

Apart from the difference in bandgap energies for different semiconductor materials, the bandgap can also be classified into direct and indirect bandgap(figure 7 [7]). As the name implies, direct bandgap materials require only energy of the photon to excite the electron to the conduction state, whereas for indirect bandgap materials additional momentum is also required.
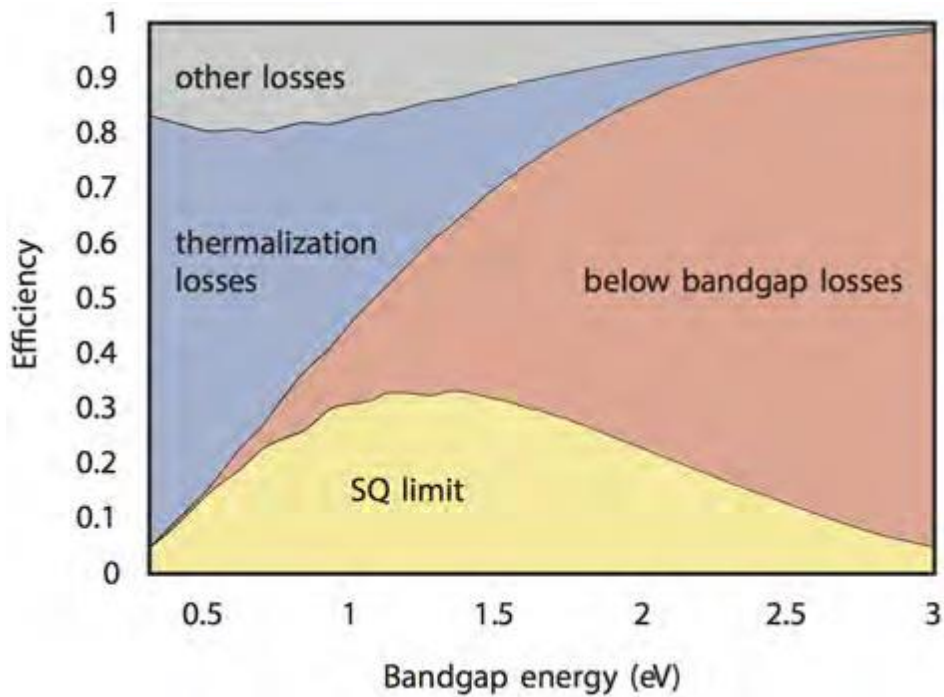
Figure 6: Major loss mechanisms in Shockley Queisser limit.

Generation of charge carriers is said to be successful when the absorbed light results in formation of electron-hole pair in the conduction and valence bands respectively. An electric field created by the doped layers guide the charge carriers towards the collector. The electrons and holes are then recombined at the two electrodes which connect via an external circuit. The concentration of the collected charge carriers gives the potential of the device.
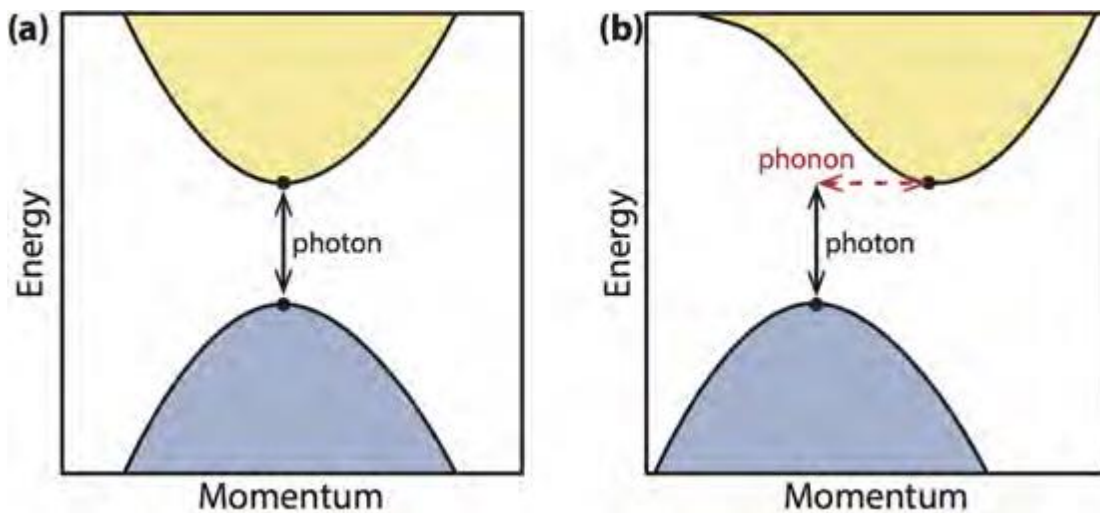
Figure 7: a) Direct Bandgap Semiconductor; b) Indirect Bandgap Semiconductor.
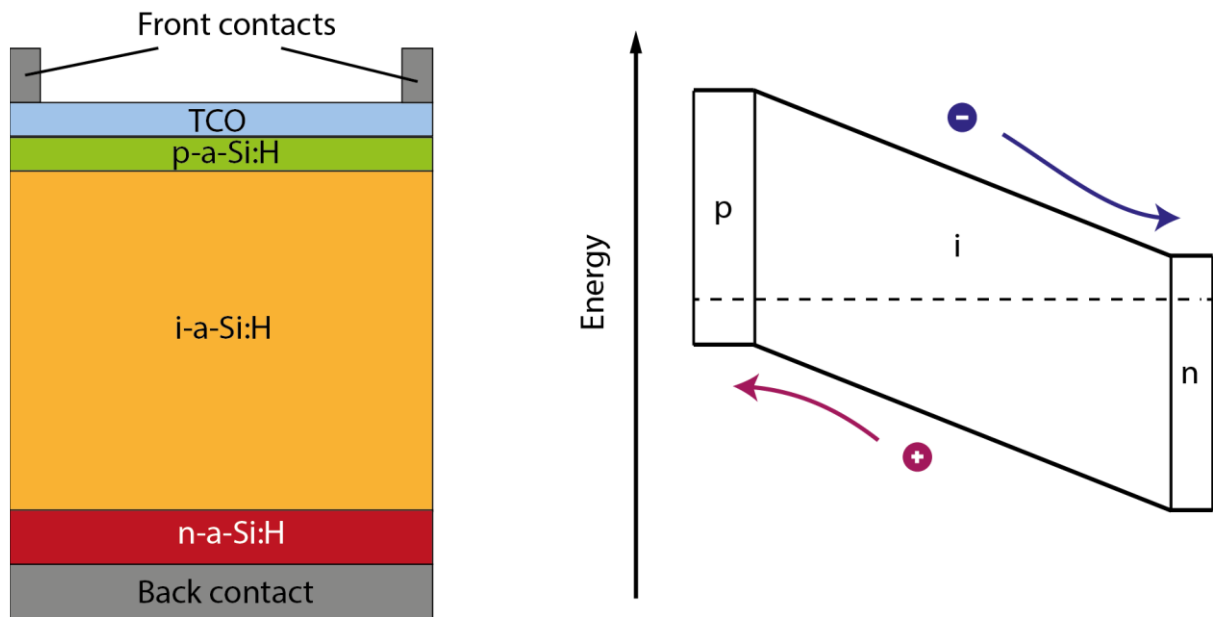
Figure 8: Structure of a n-i-p solar cell with corresponding energy bandgap diagram

Crystalline Silicon(c-Si) is one of the first generation of Photovoltaic (PV) technologies which have been researched for the past 5-6 decades. Solar cells made from c-Si have a thickness of about 160-300µm. Manufacturing of high purity of c-Si materials is expensive, which paves way to search for cheaper and more flexible materials. The second generation of PV technologies are the Thin-Film Silicon Solar cells (TFSSC). In comparison with the first-generation c-Si cells, TFSSC are much thinner in the range of about a few hundred nanometres. These devices are generally called drift devices since the charge carriers are transported to the contacts by the electric field generated in the junction.

1.3 Thin Film amorphous silicon solar cell

A generic structure of an amorphous silicon thin film solar cell is shown in figure 8 [8]. There are 2 different classifications namely *p-i-n* and *n-i-p* which can be configured in superstrate or substrate. The commonly used configurations are *p-i-n* superstrate structure and *n-i-p* substrate structure where the p-layer acts as the window layer. The difference between the two is the order of layer deposition. In a *p-i-n* structure the substrate is a transparent substrate usually glass with a TCO coating on which p-doped layer is deposited followed by the intrinsic and n-doped layer. In a *n-i-p* substrate structure the fabrication is in reverse order and the substrate can be a textured metal or a crystalline Si wafer. In both the configurations, the light enters through the p-layer which is one of the important layers in determining the overall performance of an a-Si based solar cell device [9, 10]. Thin film Silicon Solar cells are fabricated in a layer by layer process called Plasma Enhanced Chemical Vapour Deposition (PECVD) at low temperatures (200°C-300°C) on a mechanically strong materials like glass, aluminium or a polymer. The properties of the layers can be fine-tuned by controlling the various deposition parameters of PECVD process like the flow rate of the precursor gases, the power, pressure and temperature to name a few.

The Staebler and Wronski effect is the light induced degradation in the material properties of the hydrogenated amorphous silicon (a-Si:H) which limits the performance of the thin film silicon solar cells. Although the exact mechanism of the defects induced by this effect has not been established but, recently a hypothesis was put forward which assigns trap-assisted auger recombination as the dominant recombination process [11]. Another limitation of a thin film silicon solar is the limited spectral response. As seen in figure 6, low bandgap materials suffer from thermalization losses whereas high bandgap materials have non absorption losses. A tandem solar structure with cells with decreasing bandgap with reference to the incident light will result in lower spectral losses. With this as a motivation, a tandem solar cell is developed with the required voltage to smoothly carry out electrolysis of water to produce hydrogen for use as fuel or as a precursor to chemical fuel.

1.4 Aim and Outline of this Thesis

Since the incident light is passing through the p-doped layer, it is crucial to design and deposit the layer optimizing the optical and electrical properties. One of the challenges is to develop a basic working *n-i-p* substrate solar cell on a glass substrate. The parameters which determines the performance of the cell is the $V_{oc} \times FF$ product and efficiency while the J_{sc} can be tuned to with respect to the subsequent bottom cells. The scope of this thesis is to investigate the hydrogen plasma treatment between the i/p and p/TCO interface of an a-Si cell and optimal deposition conditions for the window layer of the a-Si cell are to be derived iteratively.

The research questions for this thesis can be formulated as follows:
1. Does Hydrogen Plasma Treatment (HPT) have any effect between the layer interfaces? (Challenge: To find the morphological and intrinsic properties of the layers affected by HPT)
2. What are the trade-offs and trends in varying the properties of the p-nc-SiO$_x$? (Challenge: To balance the optical and electrical properties)
3. What are the trade-offs and trends in varying the thickness of the contact layer and the TCO? (Challenge: To find a balance between the optical properties)
4. What changes in the absorber layer can generate a current matched 2-junctino solar cell? (Challenge: Iterate the thickness of the high bandgap top cell and the band structure of the bottom cell)

With the preliminary introduction to the topics already covered in this chapter, the structure of this report is further described as per the progress of the experiments. Chapter 2 elaborates on the various properties of the materials. Chapter 3 describes the flow of the experiments as performed and the measurement techniques used to characterise the performance of the layers and the solar cell. Chapter 4 investigates the effects of Hydrogen Plasma Treatment in the i/p interface and the p/TCO interface. Chapter 5 details on the balance of the effects of the deposition parameters in the p-layer stack. Chapter 6 presents a test series of 2 junction tandem solar cells with a-Si as the top cell and SiGe as the bottom layer. The final chapter outlines and summarizes on the optimal parameters or a likely trend to customise the device based on the specific requirement and provides some recommendations for future work/alternatives.

2.Theoretical Background

This chapter provides information on the semiconductor device physics and intrinsic properties of the materials used in this work and the external parameters of PV device.

2.1 Optical Properties

Visible light is a part of the electromagnetic spectrum emitted from the surface of the sun. The electromagnetic theory describes the propagation of light as wave. The relation between the wavelength and energy of light and its behaviour at the interface of two materials and/ inside a certain material can be illustrated by their optical properties.

2.1.1 Interaction at interface

The speed of light varies in different mediums as per the density of the medium. Due to this difference, a fraction of light at the interface of two media may be reflected and transmitted. The ratio of the speed of light in vacuum with the speed of light in a medium gives the refractive index of the medium (n).
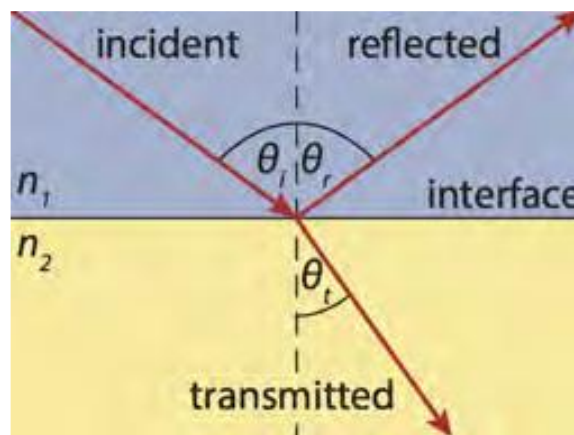
Figure 9: Light behaviour at the interface of 2 mediums [7]

The angle of incidence is the angle of the incident ray of light with respect to the normal of the interface and is equal to the angle of reflection. The relation between angle of incidence and angle of transmission is described by Snell's law,

$$\frac{n_1}{n_2} = \frac{\sin(\theta_t)}{\sin(\theta_i)}$$

(2.1)

Where, n_1 is the refractive index of the first medium,
n_2 is the refractive index of the second medium,
θ_i is the angle of incidence,
θ_t is the angle of transmission.

An electromagnetic wave consists of perpendicular electric and magnetic fields and they are orthogonal to the direction of wave propagation. Polarization is a term used to describe the orientation of the electric field of the wave with respect to the plane of incidence. When the plane of electric field is perpendicular to the plane of incidence, it is said to be s-polarised while when the electric field is parallel to the incident plane, it is called p-polarised. The relation between the incident, reflected and transmitted waves are given by Fresnel's equations.

For s-polarised light,

$$t_s = \frac{2n_1 cos\theta_i}{n_1 cos\theta_i + n_2 cos\theta_t} \tag{2.2}$$

$$r_s = \frac{n_1 cos\theta_i - n_2 cos\theta_t}{n_1 cos\theta_i + n_2 cos\theta_t} \tag{2.3}$$

For p-polarised light,

$$t_p = \frac{2n_1 cos\theta_i}{n_1 cos\theta_t + n_2 cos\theta_i} \tag{2.4}$$

$$r_p = \frac{n_1 cos\theta_t - n_2 cos\theta_i}{n_1 cos\theta_t + n_2 cos\theta_i} \tag{2.5}$$

Where, t_s is the transmitted wave for s-polarised light
r_s is the reflected wave for s-polarised light
t_p is the transmitted wave for p-polarised light
r_p is the reflected wave for p-polarised light

Since the sunlight is unpolarised light, the effective reflectivity can be obtained by the mean of the two polarization.

$$R = \frac{1}{2}(r_s^2 + r_p^2) \tag{2.6}$$

Assuming the mediums to be non-absorbing in nature, the energy conservation law states that the sum of reflection and transmission is 1.

$$1 = R + T \tag{2.6}$$

2.1.2 Absorptive medium

While traversing through a medium, a part of the light is absorbed if the energy of the photon is greater than the energy required for electron excitation. Thus, the updated form of equation 2.6 is given as,

$$1 = R + T + A \tag{2.7}$$

Where, A is the amount of absorbed light

The refractive index n is the real part of the complex refractive index (n+iκ). κ is the imaginary part of the refractive index also known as the wave number. While traversing through a

medium, the intensity of the electromagnetic field attenuates with respect to the distance travelled in the medium. This attenuation is given by Lambert-Beer law.

$$I(x) = I_0 \, exp(-\alpha x) \tag{2.8}$$

Where, I is the intensity of the EM wave,
x is the distance travelled in the medium,
α is the absorption coefficient.
The relation between α and wavenumber is given by,

$$\alpha = \frac{4\pi\kappa}{\lambda} \tag{2.9}$$

Where, λ is the wavelength of the light.

2.2 Electrical Properties

After absorption of light, the generated electron hole pairs in the absorber layer are separated and collected at the two contacts.

2.2.1 Conductivity

The flow of charge carriers between two contact depends on the resistance of the material and the voltage applied at the contacts. This resistance is given by ohm's law,

$$R = \frac{V}{I} \tag{2.10}$$

Where, V is potential difference in volts,
I is current in amps
R is resistance in ohm

The volumetric resistance or specific electrical resistance is defined as the ease of conduction of current for a specific length of material across a unit cross-section. It is also called resistivity and defined by the formula,

$$\rho = R\frac{l}{A} \tag{2.11}$$

Where, ρ is resistivity in ohm.m,
l is length in m
A is cross sectional area in m^2
R is resistance in ohm

The reciprocal of resistivity is conductivity (σ). Metals have high conductivity while insulators have the lowest conductivity. While mixed phase semiconductor materials have variable anisotropic conductivity. Anisotropic conductivity refers to difference in conductivity with respect to the direction of current. For PV devices, semiconductor materials should have high transverse conductivity. One of the material characterizations is describing the electrical conductivity with respect to the temperature.

2.2.2 Activation Energy

The energy required to excite an electron from its valence state to conduction state is called activation energy (E_A). The lower the activation energy, the easier it is to excite an electron to conducting state. The relation between conductivity and activation energy is given by Arrhenius's equation:

$$\sigma = \sigma_0 \exp(\frac{-E_A}{k_B T}) \tag{2.12}$$

where, σ_0 is the material dependent conductivity constant,
k_B is the Boltzmann constant,
T is temperature in Kelvin.

2.3 Material Properties

The tuneable properties of silicon and its alloys make them a preferred choice of research for PV application. The basic silicon lattice structure and its limitations will be discussed in this segment.

2.3.1 Lattice structure/morphology

The atomic structure/lattice structure defines the intrinsic properties of the materials. Silicon exists in many phases namely, crystalline, micro-crystalline and amorphous. The atoms in a lattice have a specific geometric arrangement whose order over molecular distances determine the grain size of a crystal. In crystalline form, the atoms are arranged in a diamond-like tetrahedral structure having a varying grain size. The unbonded silicon atoms also called dangling bonds are present on the surface edges of the material. In amorphous silicon the grain size is of a few atomic distances thus resulting in a large number of dangling bonds. These bonds are indicated by the defect density and are often passivated by hydrogen.
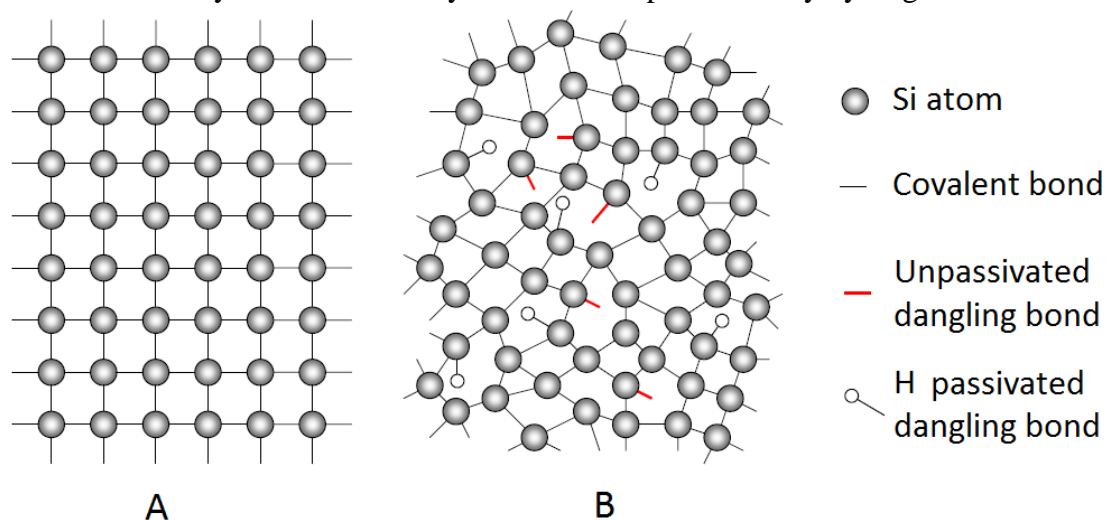
Figure 10: Lattice structure of A. c-Si; B. a-Si [12]

A-Si and micro.c-Si can be produced by Plasma Enhanced Chemical Vapour Deposition (PECVD), which will be discussed in chapter 3. The bandgap energy of a-Si ranges from 1.6-

1.8 eV while that of c-Si is around 1.12 eV. The long order grains of c-Si make it more conductive than a-Si, but the small bandgap also increases the losses in the form of thermalisation. The process parameters have a great influence on the morphology of the deposited silicon.

The figure 11 showcases the change in morphology of a-Si with respect to PECVD parameters like silane concentration, plasma power, frequency, temperature and even substrate. Doped semiconductors can also be fabricated with the introduction of the specific dopant gases. The mixed phase material SiO_x, formed by introduction of oxygen atoms in the a-Si, has relatively high optical transparency with larger grains of crystals compared to a-Si. The silicon crystals embedded in the amorphous nc-SiO_x gives it better transverse conductivity. SiO_x also has a larger bandgap and lower absorption which makes it ideal for the window layer. A-Si and SiO_x also suffer from some drawbacks.
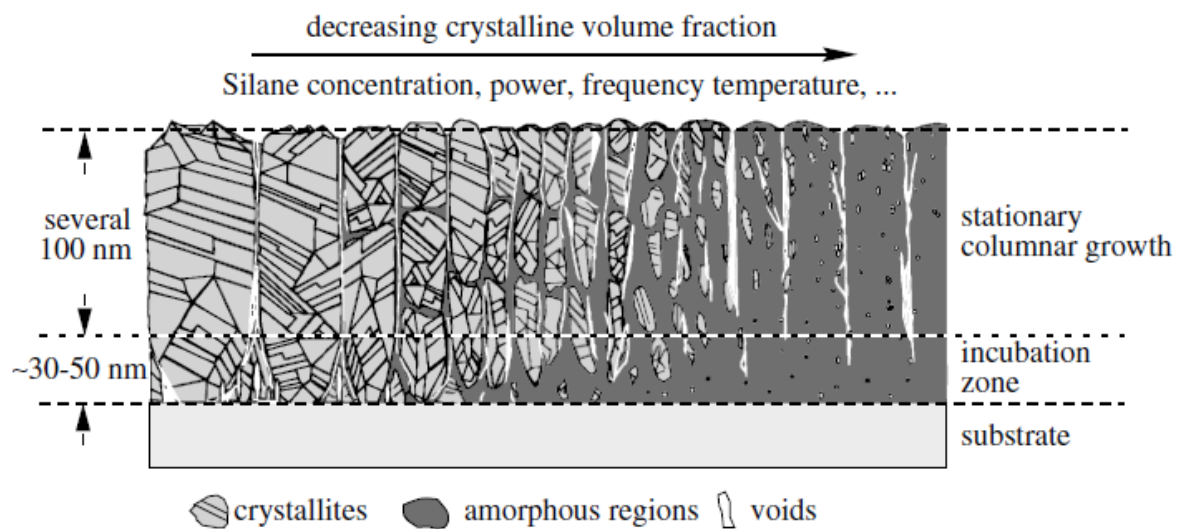
Figure 11:Phase change a-Si to poly-Si [13]

2.3.2 Drawbacks/defects

On exposure to light the weaker bonds in a-Si are broken thereby creating new dangling bonds. This is light induced degradation (LID) which is also known as Staebler-Wronski effect. This effect can be reversed by annealing the material at temperatures around 150°C for a few minutes. As a rule of thumb, the higher the temperature, the higher is the reversal rate. The higher the intensity of light, the higher is the number of dangling bonds. An equilibrium between these two phenomena can be reached after 1000 hours of light exposure.
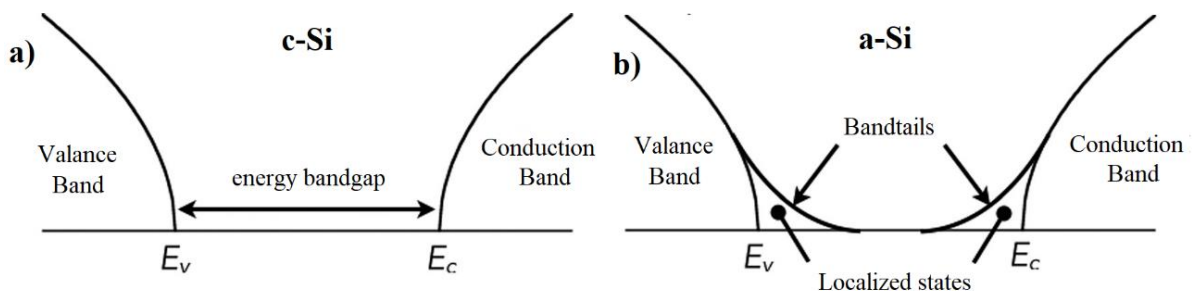
Figure 12: DOS distribution of a) c-Si; b) a-Si [14]

Disorder in amorphous silicon creates variations in bond angle and bond length, thus giving rise to bandtails states in the valence and conduction band border regions as seen in figure 12. The edges of valance and conduction bands are well defined in high purity crystalline silicon whereas in amorphous silicon the density of states decrease exponentially till the middle of bandgap. The large number of defects reduces the charge carrier lifetime.

Lattice defects, including interstitial voids and substitution by impurity atoms such as boron, are introduced during the processing of the materials. The voids formed in the amorphous silicon results in an increase in dangling bonds. These bonds act as recombination centres or traps centres. The recombination of the photo-generated charged carriers prevents them from reaching the contacts and the not contribute to the energy generation.

3. Experimental Methodology

The substrate configuration *n-i-p* a-Si solar cells have been fabricated in the clean room 10000 of the Else Kooi Laboratory at TU Delft. The cluster machine used is called AMIGO which uses PECVD for semiconductor layer deposition. This chapter is divided into two parts: the first part describes the equipment used for sample fabrication, and the second part gives information on the characterization equipments.

3.1 Fabrication Techniques

In this work, Asahi glass with TCO was used as the substrate for solar cell depositions while flat Corning glass was used for testing optical and electrical properties of individual layers of interest. The structure of the solar cell is as follows: Asahi Glass / FTO / AZO / n-nc-Si:H / n-a-Si / i-a-Si / i-nc-Si / p-nc-SiO$_x$ / p-nc-Si / ITO / metal grid. Before placing the Asahi glass inside AMIGO, the glass substrate is cleaned in subsequent ultrasonic bath of acetone and isopropanol (IPA) for 10 minutes each. The ultrasonic cleaning process creates bubbles in the solution which interacts with the impurities and dust particles effectively deep cleaning the surface of the substrate.

3.1.1 Plasma Enhanced Chemical Vapour Deposition

Chemical Vapour Deposition (CVD) is a process where dissociation of suitable reaction/precursor gasses at a specific temperature results in the formation of a solid thin films of the material. The temperature for bond breaking of the gasses in a CVD is around 600°C. The use of radio frequency plasma enhanced CVD (rf-PECVD) helps in reduction of the temperature by half. The plasma is created by alternating voltage at the two electrodes with a frequency of 13.56 MHz or 40 MHz. A schematic diagram of a simple PECVD reaction chamber is shown in figure 13.
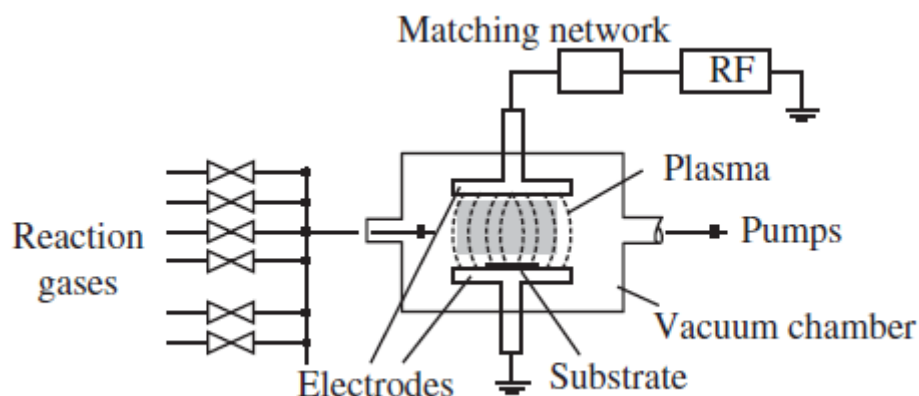
Figure 13: Schematics of PECVD.[13]

The reaction chamber is maintained at high vacuum by the turbo-molecular pump and the temperature is controlled with the help of a heater. The importance of high vacuum is to avoid any impurities or dust particles and ensure a smooth layer of material deposition. The precursor gasses are regulated with a mass controller to control the amount of doping (diborane or phosphine) or hydrogenation (hydrogen) or just to deposit intrinsic material (silane or germane). To make alloys like SiO_x silane and carbon dioxide are used while, to make SiC silane and methane are used in conjunction with hydrogen. The cleaned samples are placed in cleaned holders which are heated to the desired temperature in the chamber and placed on one of the electrodes which is grounded. The other electrode is fed alternating voltage as per the requirement of the material growth at a radio frequency. The alternating voltage creates an oscillating electric field. This electric field causes the light electrons of the gas molecules to knock off the orbitals and create heavier positive gas ions. Since the oscillation is at a high frequency, the positive radicals become the plasma and attach to the substrate which is grounded. A successful plasma is produced when the gasses break down into positive ions and electrons with a sufficient bias voltage. The power and pressure mainly defines the force with which the ions interact with the substrate. Increasing power may increase the deposition rate but after a threshold the excessive ion bombardment may result in etching of the material. High pressure of gasses increases the total number of molecules in the chamber which increases the collision between the ions resulting in fewer reaction at the substrate. This results in a lower deposition rate. Thus, it can be stated that the quality/properties of the material deposited is dependent on multiple confounding variables. The deposition of p-doped layer, n-doped layer and intrinsic layer was performed in separate chambers of AMIGO to minimize contamination.

Influential of deposition parameters are:

1. Power
2. Pressure
3. Temperature
4. Gas Flow rates
5. Time of deposition

3.1.2 Magnetron Sputtering

The protective AZO layer on the substrate and the TCO layer at the front after p-doped layer are deposited by the process of magnetron sputtering. A typical RF magnetron sputtering system has a cathode, which acts as electron emitter, attached to the target while the sample is attached to the anode in a vacuum heated chamber. A plasma is formed due to an alternating electromagnetic field in presence of a noble gas like argon. The argon ions bombard the target surface and the oscillating field transfers the atoms to the sample. A schematic layout of RF magnetron sputtering used in EKL is shown in figure 14. The sample is rotated inside the chamber to have control over the uniformity of deposition.

For AZO deposition a ceramic target of 2% Al_2O_3 and 98% of ZnO by weight is used. While ITO target consisting of 10% SnO_2 and 90% In_2O by weight is used as a TCO.
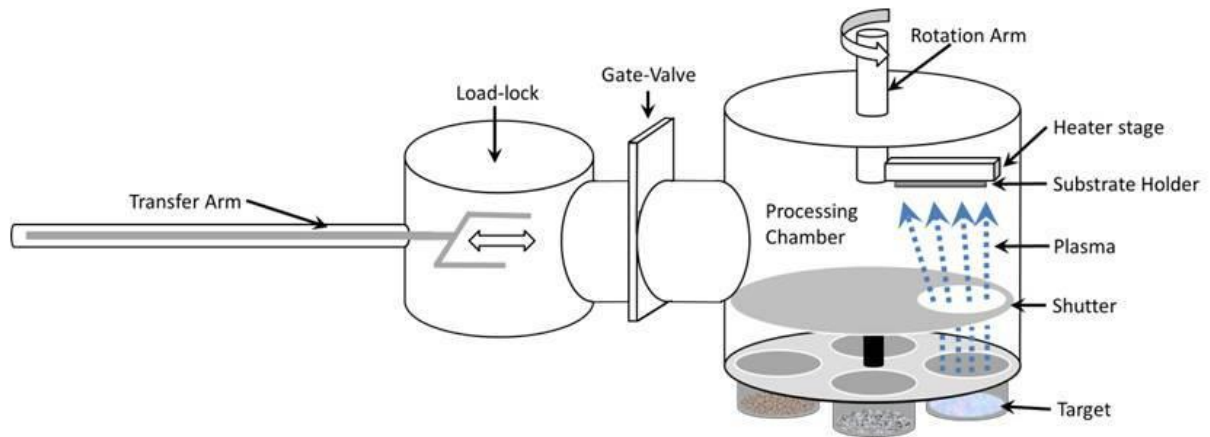
Figure 14: Schematics of magnetron sputtering [15]

3.1.3 Metal Evaporation

The contacts on the solar cells made in this work are thin films of aluminium. A grid format is used to maximize the light throughput and collection of charged carriers. The TCO on the substrate is used as the back contact while the Al metal grid with a 500nm thickness forms the front contact. The deposition was carried out by metal evaporation technique. Thermal and electron beam are the two different methods of metal evaporation. In thermal metal evaporation, low boiling point metals like Ag, are heated by passing a high current through the crucible while in the electron beam method, a stream of electrons with high kinetic energy is targeted at the metal which vaporises the metal and deposits it on the substrate.
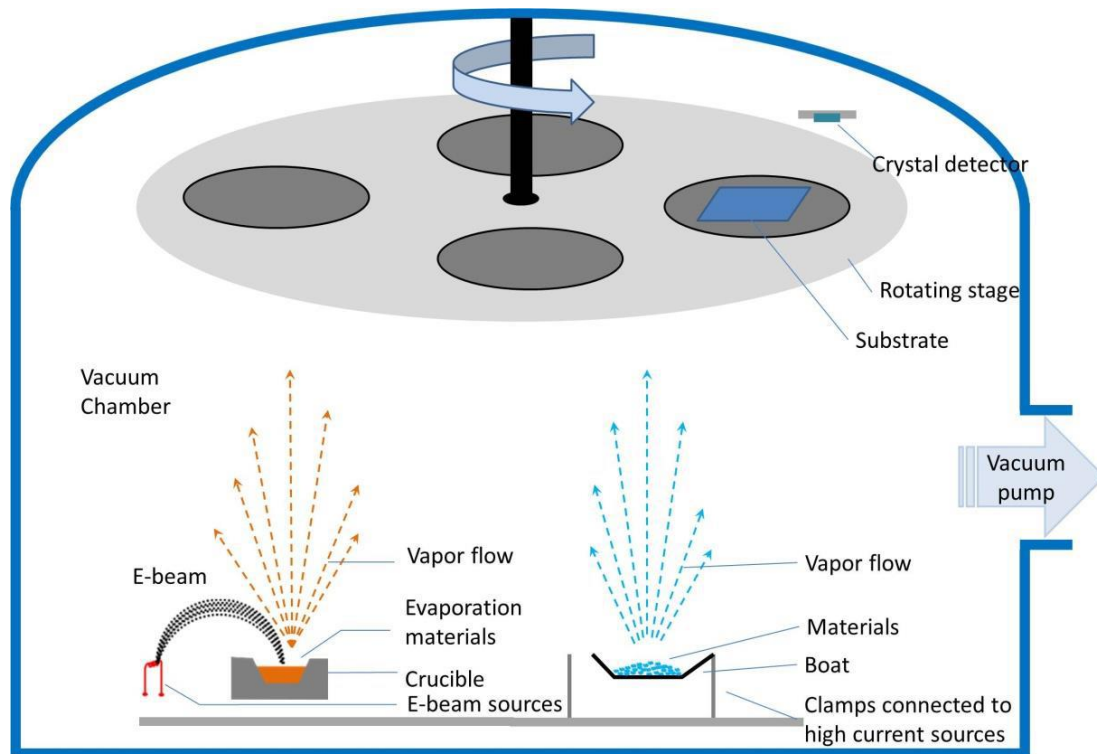
Figure 15: A Schematics of metal evaporation chamber for depositing thin film metals [15]

17

3.2 Characterization Techniques

The characterisation of the performance of a solar cell is based on the open circuit voltage (V_{oc}), short circuit current (J_{sc}), fill factor (FF), external quantum efficiency (EQE) and the transmission reflection absorption (TRA) curve. These parameters are then used to calculate the efficiency of the cell. To study the material properties of a single layer, a test sample is created by depositing the test material onto a corning glass substrate with flat morphology.

3.2.1 JV curve measurements

The current density vs voltage curve (JV curve) gives an overall view of the solar cell parameters like short circuit current, open circuit voltage, FF and efficiency. To perform reproducible measurements, a set of standard test conditions are followed: solar cell temperature should be 25°C, the spectrum of light should be equivalent to AM1.5 and the total irradiation should be equal to 1000W/m^2.

The solar cell to be measured is connected to a variable load and the current produced at different voltages are plotted. The V_{oc} and J_{sc} are the x and y intercepts of the curve, while the other external parameters can be derived subsequently. The figure shows a typical JV curve of a solar cell.
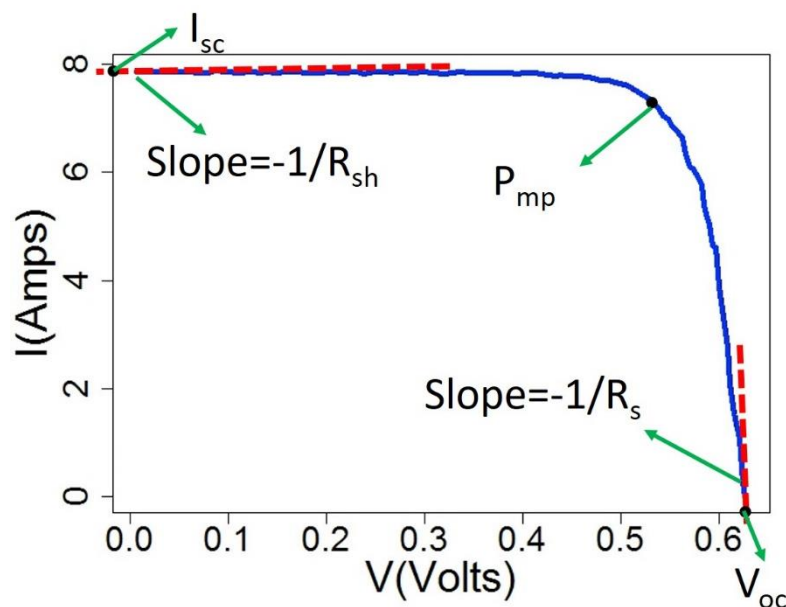
Figure 16: A typical JV curve of a solar cell [16]

The equipment used in this work is a Wacom WXS-16-L2 Solar simulator which is calibrated using reference c-Si solar cells from Fraunhofer Institute of Solar Energy Systems. A separate EQE setup is used for accurately measuring the current density.

3.2.2 EQE measurements

External Quantum Efficiency (EQE) is defined as the ratio of the number of incident photons to the number of successfully collected electron-hole pairs. It is measured by illuminating the

solar cell with monochromatic light of wavelength λ and the photocurrent. The EQE is then calculated by:

$$EQE(\lambda) = \frac{I_{ph}(\lambda)}{q\Psi_{ph,\lambda}} \qquad (3.1)$$

where, $\Psi_{ph,\lambda}$ is the spectral photon flux.

The EQE setup is calibrated using a silicon photodiode and reading of the photocurrent is recorded in steps of 10nm. The integral of $I_{ph}(\lambda)$ over the required spectral range (300nm-850nm) gives a reliable J_{sc} of the solar cell.

$$J_{sc} = \int_{\lambda_1}^{\lambda_2} I_{ph}(\lambda)d\lambda \qquad (3.2)$$

A complete spectral analysis is done by comparing the EQE with the intensity of light absorbed by the cell. As seen in fig 17, the area enclosed between the two curves represent the collection losses while the area above the black curve represents the reflection and transmission losses.
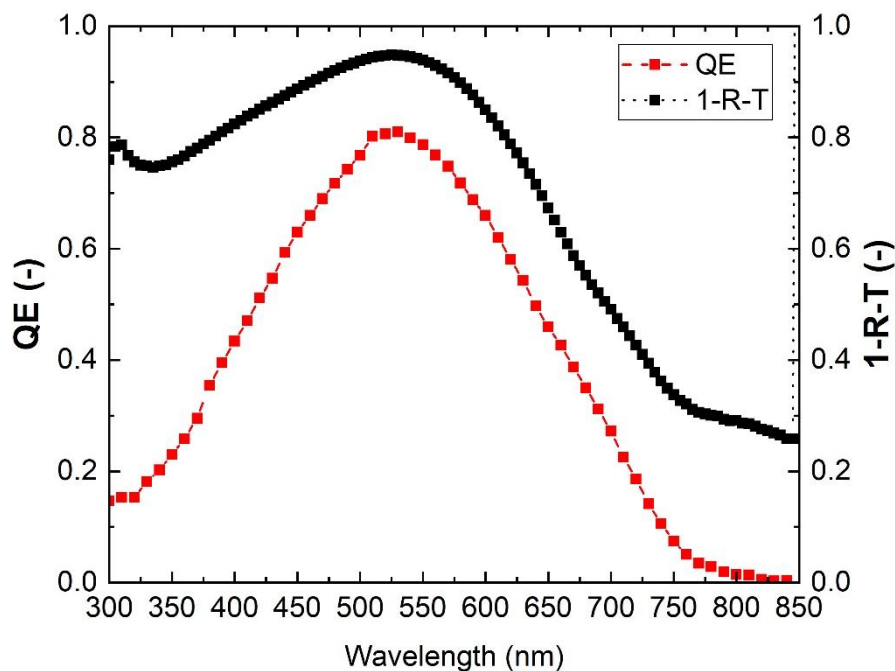
Figure 17: EQE and absorption graph

3.2.3 Dark Conductance measurements

The energy states in the band gap can be detrimental to the performance and electronic properties of solar cells. One of the methods to determine this effect is by measuring dark conductivity of the semiconductor. The determination of dark conductivity of a thin film silicon layer is carried out by measuring the J-V curves as a function of temperature in absence of light.

Conductivity of a semiconductor is given by:

$$\sigma_d = e(n\mu_n + p\mu_p) \tag{3.3}$$

Where n and p are electron and hole concentration which are dependent on temperature and the fermi level position in the band gap.

$$n = N_c \exp\left(\frac{E_F - E_C}{kT}\right) \tag{3.4}$$

$$p = N_c \exp\left(\frac{E_V - E_F}{kT}\right) \tag{3.5}$$

Where N_c and N_v are effective density of states in the conduction and valance band.

To measure the dark conductivity the sample are prepared separately. The films measured in this work are deposited on corning glass with a thickness of 10-20nm. This is followed by Al contact bars of thickness t mm, a distance of d mm and length of l mm. A thermally controlled stage is used to regulate the substrate. The temperature is varied from 130°C to 60°C with 5°C steps and the dark conductivity is measured by:

$$\sigma_d = \frac{dI}{tlV} \tag{3.6}$$

The energy required to excite electron from valance band to conduction band is known as activation energy (E_A). Slope of $\ln(\sigma_d)$ vs 1000/T of the Arrhenius plot is the activation energy which is generally a straight line for good quality films. Its relationship with the dark conductivity as by Arrhenius equation is:

$$\sigma_d(T) = \sigma_0 \exp\left(\frac{-E_A}{kT}\right) \tag{3.7}$$

Where σ_o is the pre-exponential factor.

3.2.4 Spectroscopic Ellipsometry

The thickness of layers, the absorption coefficient and refractive index are measured by spectroscopic ellipsometry. It is a non-invasive method which also provides information on the roughness of the sample by measuring the change in the polarization as light reflects from the surface. A linearly polarised light beam is incident on the surface and reflected into the analyser which determines the change in terms of an amplitude ratio and a phase difference. The measurements are carried out at an angle close to the Brewster angle of the material. The ratio of the two values are then fitted to a model to give an accurate and reliable result.

$$\tan(\Psi)\, e^\Delta = \rho = \frac{r_p}{r_s} \tag{3.8}$$

Where Ψ is the amplitude ratio,
Δ is the phase difference,
r_p and r_s are the reflectivity of p-polarised light and reflectivity of s-polarised light respectively.
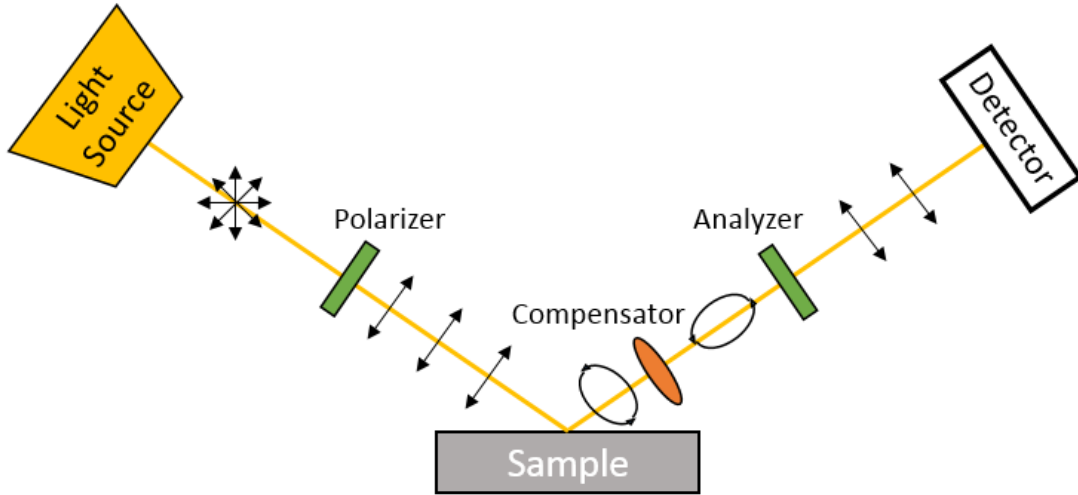
Figure 18: Spectroscopic ellipsometry (SE) measurement schematics [17]

3.2.5 Raman Spectroscopy

Structural characterization of silicon is performed by Raman spectroscopy. The guiding principle is the frequency shift resulting from the scattering of incident light due to collision with the lattice atoms of the material to be studied. This interaction of photons with the lattice gives insight into the atomic structure and bonding nature between the different atoms. A green laser of wavelength 514nm is used as the incident light. The wavelength and energy of the incident light is shifted up (stokes shift) or down (anti-stokes shift) due to the vibrational energy known as phonon. The difference in the intensity of the scattered light is plotted as a function of the wave number and is expressed in cm^{-1}. A peak in the raman spectrum indicates a certain silicon bond at the wavenumber. In case of silicon, a peak at 480 cm^{-1} represents an a-Si stretching mode while a peak at 512 cm-1 shows c-Si stretching bonds. Oxygen-Silicon bonds and Hydrogen silicon bonds occur at the further IR regions of the raman spectrum. The intensity at each wavenumber also gives information about the concentration of the particular bonds. The fraction of the gaussian peaks is used to calculate the crystallinity of the material.

$$X_C = \frac{I_{c-Si}}{I_{C-Si} + \gamma\, I_{a-Si}} \qquad (3.9)$$

Where, X_c is the crystalline fraction,
I_{c-Si} is the area of crystalline peak,
I_{a-Si} is the area of amorphous peak,
Γ is the correlation factor.

4. Hydrogen Plasma Treatment

4.1 Introduction

The performance of a *n-i-p* solar cell can be improved by several methods like maximal light trapping, improving the material quality of the absorber layer, and optimizing the properties of the interface. The material properties and mechanisms that influence the interface have been researched extensively for a-Si:H solar cells[15, 18, 19]. The difference between the wide band gap p-SiOx:H and the narrow bandgap of i-a-Si layer is eased at the hetero-junction interface. Another factor that has significant effect on the performance is the recombination in the interface region[20]. The high defect density due to lattice mis-match, dangling bonds, etc, result in recombination centres.

While one of the ways to optimize this interface is by introducing a buffer layer, the aim of this chapter is to showcase the influence of varying hydrogen plasma treatment conditions at the i/p (here after called "pre-HPT") and p/TCO (here after called "post-HPT") junctions on the effects on material properties and the solar cell performance. After the deposition of the intrinsic layer, the sample was transferred to a second chamber where the HPT was carried out following the deposition of p-layer. The subsequent HPT is also carried out in the same chamber after the p-layer deposition.

4.2 Experimental setup

Single junction *n-i-p* a-Si solar cells were fabricated on a TCO coated Asahi glass. The structure of the cell as seen in figure 19 is as follows: Asahi Glass/ FTO/ protective AZO/ n-nc-Si/ n-a-Si/ i-a-Si/ i-nc-Si (seed layer)/ p-SiO$_x$/ p-nc-Si/ ITO/ metal grid. The cell was fabricated in the PECVD cluster tool AMIGO at heated chamber temperature of 300°C followed by sputtering of an ITO layer. This ITO formed the window which defined the cell area of 0.25cm^2 with 24 cells on a sample.

The effect of HPT at the two interfaces are investigated individually at first and then their combined effect is observed by analysing the external parameters. The rf power during the HPT is varied from 0W to 12W while keeping the pressure at 2.6 mBar and time at 120 sec. The next series is performed by keeping the power constant at 8W, the time constant at 120 sec and the pressure is varied from 1.2 mBar to 5.2 mBar in steps of 1 mBar. This series is followed by varying the duration of the plasma exposure from 0 sec to 240 sec. Lastly the effect of pre-HPT, post-HPT and both are compared.

Post fabrication the cells were annealed at 130°C in an oven and then the external parameters were measured. The illuminated J-V curve was performed under AM1.5 and the external quantum efficiency was measured with a monochromatic light with 0V bias and no bias light. The J$_{sc}$ from the EQE has been used to recalculate the efficiency of the device. The results

showcased are an average of 3-5 top performing cells on a sample. Appropriate adjustments have been made to compensate for the itching of the base layer due to HPT.
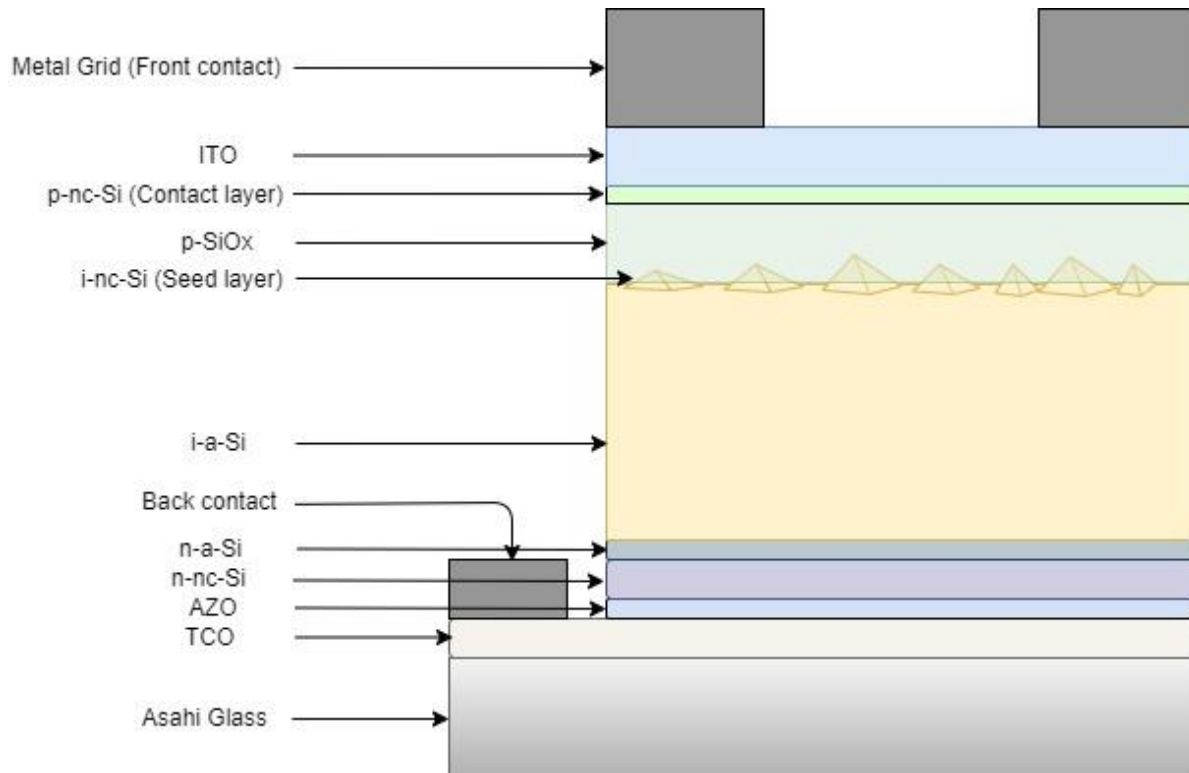
Figure 19: Schematics representation of the layers of n-i-p solar cell.

Table: 4.1: The deposition parameters for the i-p layers of n-i-p a-Si solar cell.

Parameters	i-a-Si	Pre-HPT	i-nc-Si	p-SiOx	p-nc-Si	Post-HPT
SiH_4 (sccm)	40	~	0.8	0.8	0.8	~
B_2H_6 (sccm) 200ppm in H_2	~	~	~	20	20	~
CO_2 (sccm)	~	~	~	2.3	~	~
H_2 (sccm)	~	200	170	170	170	200
Pressure (mBar)	0.7	Variable	2.2	2.2	2.2	Variable
Power (W)	2.8	Variable	35	12	35	Variable
Time (sec)	1920	Variable	150	300	54	Variable
Thickness (nm)	250	~	9	9	3	~

To further investigate the material properties, a series of thin 10-20 nm i-a-Si was deposited on corning glass and HPT was performed at different power and exposure time. Spectroscopic ellipsometry measurements were performed to check for the thickness, surface roughness and optical properties of the layers. Raman spectroscopy was performed to look into the changes in the bonding structure of the material. Metal contacts were sputtered on top for measurement of dark conductivity and activation energy.

4.3 Results and Discussion

4.3.1 Effect of power

On analysing the performance of the solar cell treated individually for different power of pre-HPT and post-HPT, the results seem to be inconclusive. A flow chart resembling the chemical reactions in a PECVD is shown in figure 20. In a PECVD reactor, the rf power affects the number of free electrons, ions and radicals which are dissociated from the precursor gasses. This potential difference is given by the energy distribution of the electrons and ions that are influenced by the electric fields between the electrodes. The electrons being much lighter and having higher velocities, tend to sway between the electrodes more than the heavier ions and radicals. To maintain the charge neutrality of the plasma, a sheath of cations is formed near the electrode. This blanket of ions varies in thickness depending on the frequency of the voltage. The thinner the sheath, the less ion bombardment on the substrate[13].
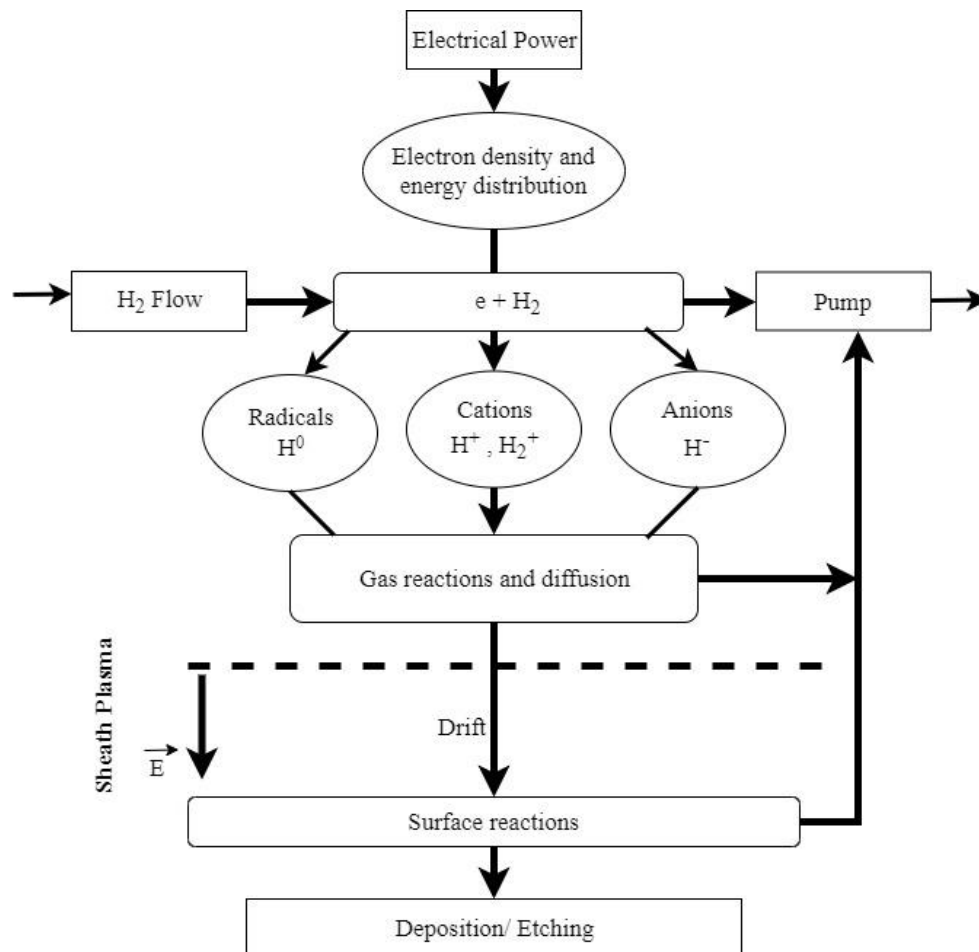
Figure 20: Flow chart of the reactions of PECVD

The external parameters do not vary more than 1% of the untreated sample. However, the performance of the cell when both the HPT are performed shows slight improvement in the higher power range.
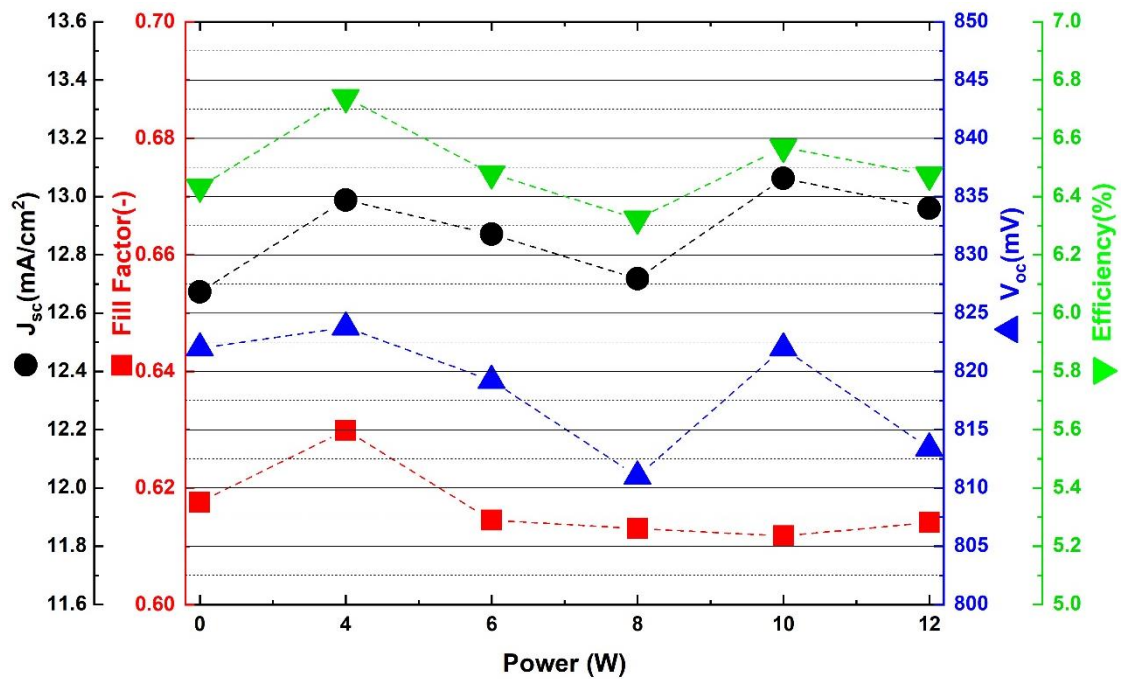
Figure 21: External parameters of solar cell as a function of power for pre-HPT with pressure of 2.6mBar and exposure time of 120seconds.
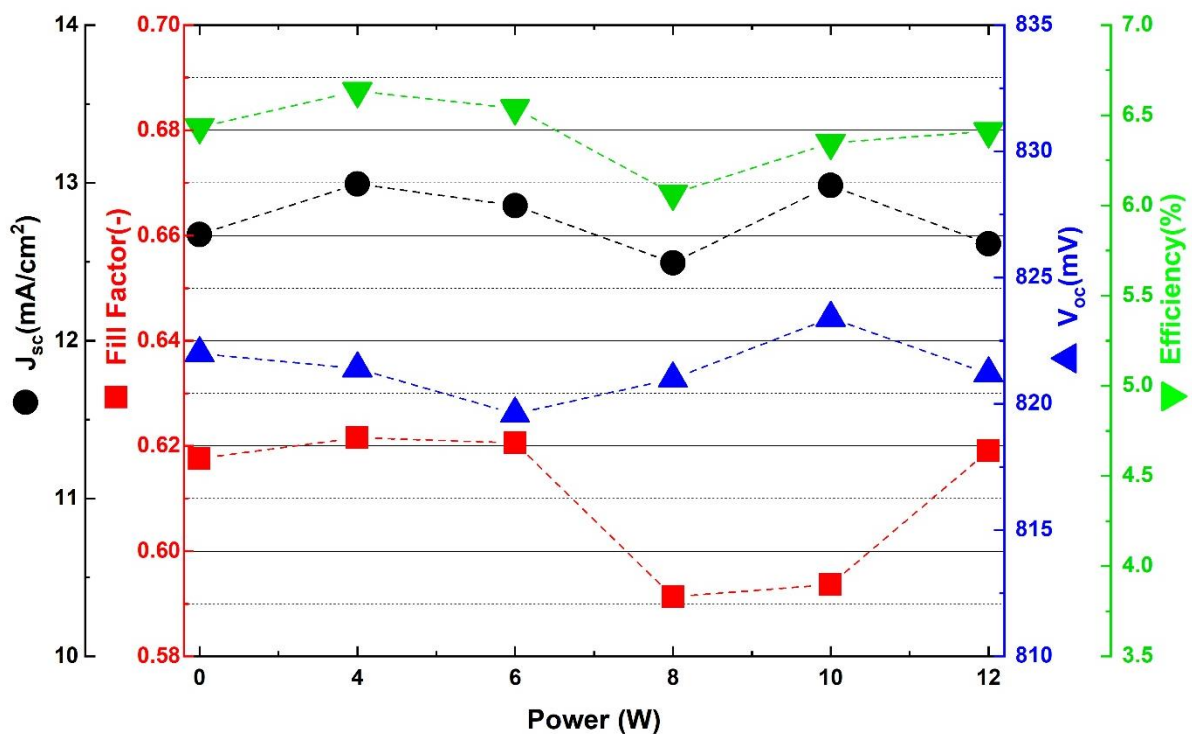
Figure 22: External parameters of solar cell as a function of power for post-HPT with pressure of 2.6mBar and exposure time of 120seconds
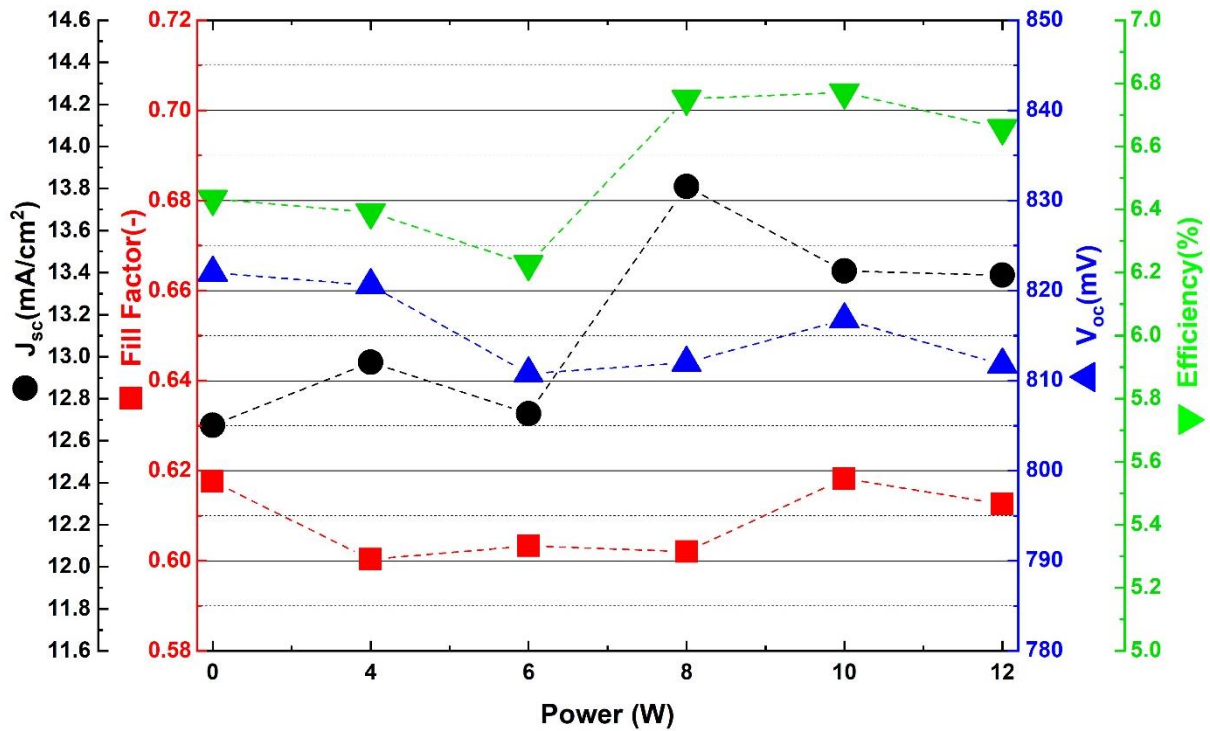
Figure 23: External parameters of solar cell as a function of power for pre and post HPT with pressure of 2.6mBar and exposure time of 120seconds

4.3.2 Effect of pressure

The dissociation of gas molecules in the reactor chamber is controlled by regulating the pressure, power and temperature of the gas. Increasing the pressure reduces the temperature of the plasma, thus reducing the concentration of energetic ions. The low pressure may result in an effective deposition of material and an increase in the ion-induced (hydrogen) electrons[21].
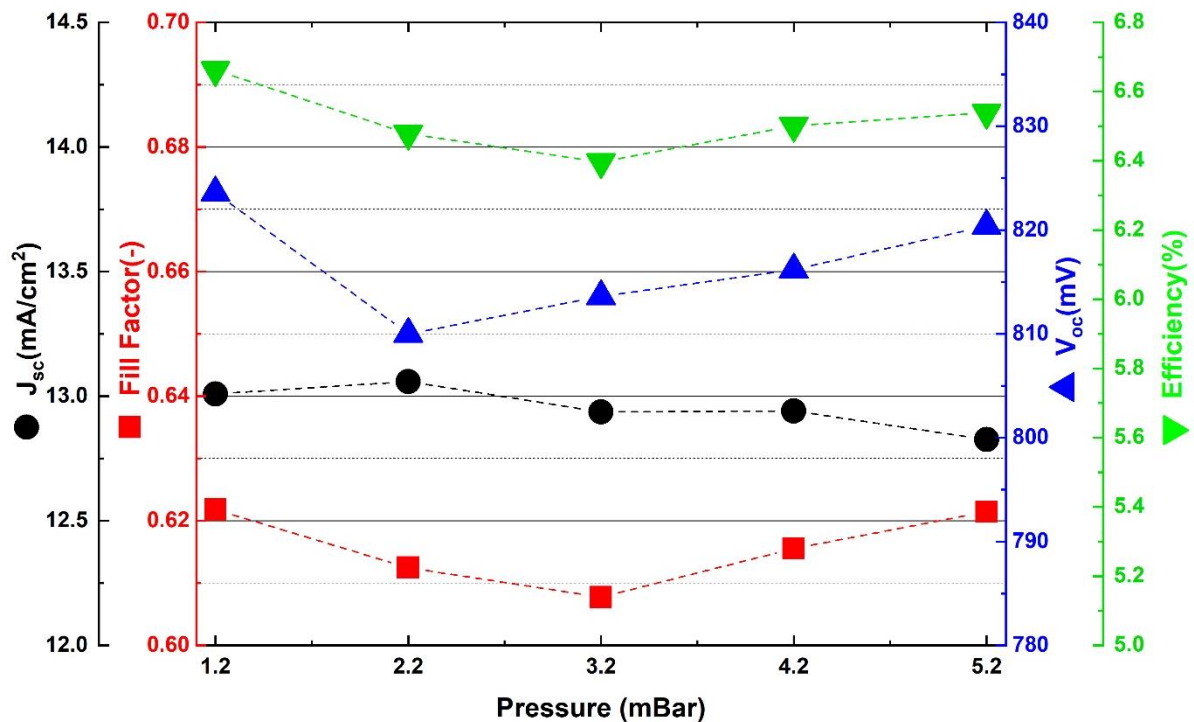
Figure 24: External parameters of solar cell as a function of pressure for pre and post HPT with power of 8W and exposure time of 120seconds

With fixed power of 8W, the lowest among the higher power range which gave high efficiency, a pressure series ranging from 1.2 mBar to 5.2 mBar showcases a better performing solar cell at lowest pressure of 1.2 mBar. To reconfirm the effectiveness of performing pre-HPT and post HPT, a set of solar cells with HPT of 8W power and 1.2 mBar pressure were fabricated. As it can be seen in figure 25 that the fill factor and current density tend to remain within a margin of 1% for post HPT and pre + post HPT. A hypothesis can be drawn that the hydrogen ions formed during the deposition of the seed layer contribute to the passivation of the dangling bonds in the i/p interface.
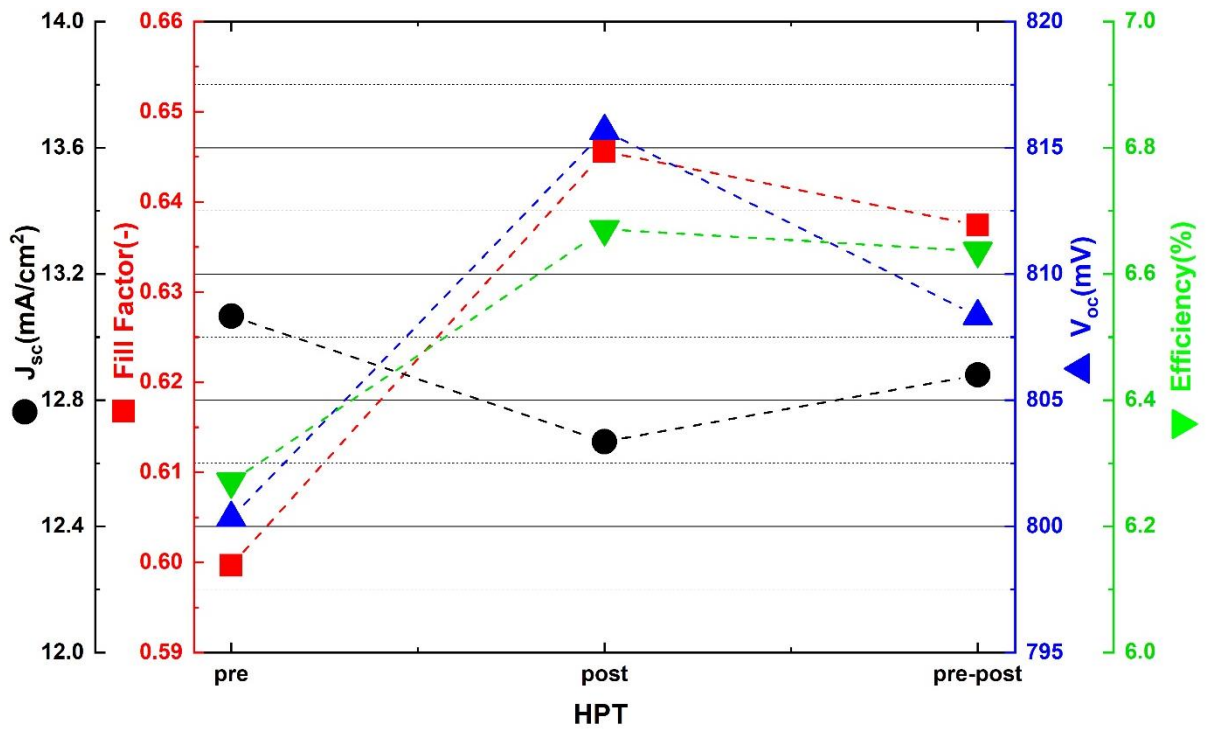
Figure 25: External parameters of solar cell for pre-HPT post HPT and pre-post HPT with a pressure of 1.2mBar, power of 8W and exposure time of 120seconds.
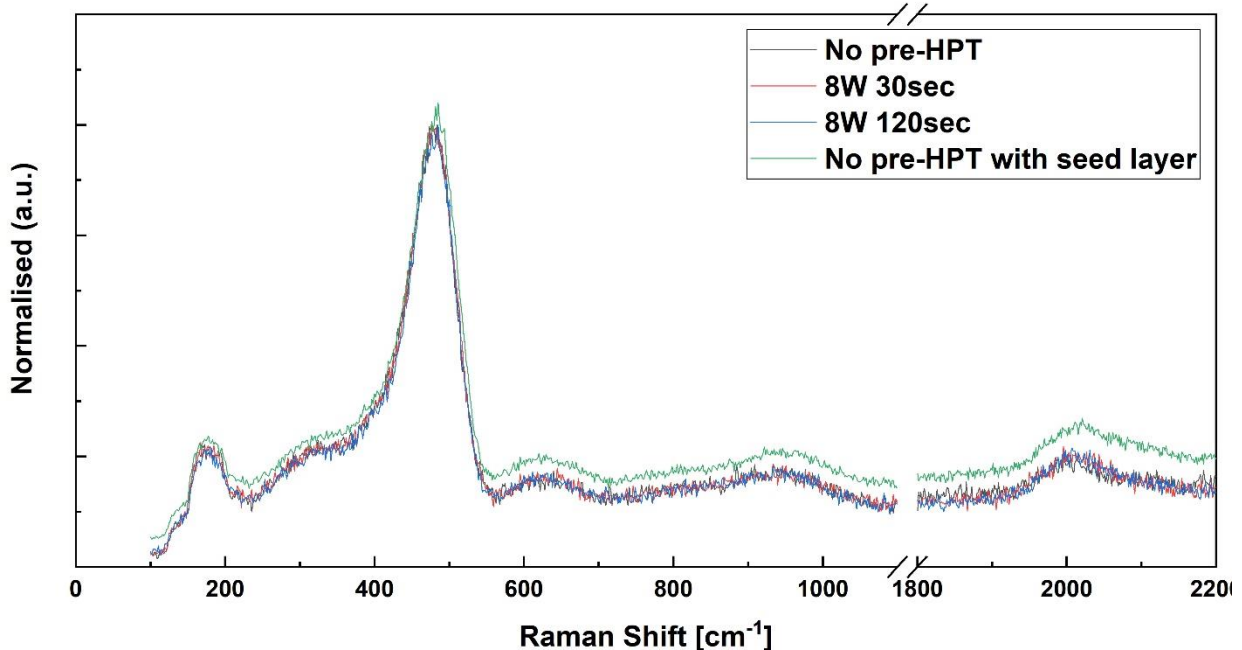
Figure 26: Raman spectroscopic analysis before and after HPT at the i/p interface.

The Raman analysis of the layers in figure 26 showcase an increase in the SiH bonds at the 2000 cm⁻¹ wavenumber for the layer of i-a-Si with a seed layer may substantiate that the effects of pre-HPT is superseded in functionality by the hydrogen dilution during the deposition of the nc-Si seed layer.

4.3.3 Effect of Time

With the optimization of the rf power and gas pressure, the next parameter to optimize the interface with HPT is the duration of the treatment. The duration of plasma exposure determines the degree of passivation of the dangling bonds by the hydrogen ions which may range from superficial passivation to the etching of the loosely bound Si bonds in a-Si layer[22]. A longer duration may result either in a thorough diffusion of hydrogen atoms into the layer material or in excessive ion bombardment resulting in detrimental effect of the HPT. Another effect of increased duration of HPT is the gradual increase in roughness of the surface[23]. The increased roughness may aid in creating seeds of nano-crystalline silicon for proper growth of p-type SiO_x.

The change in external parameters as a function of the duration of plasma exposure as seen in figure 27 shows a peak performance at 30 sec of exposure. A speculation can be made that longer duration of plasma may result in the detrimental effects of the surface instead of proper passivation.
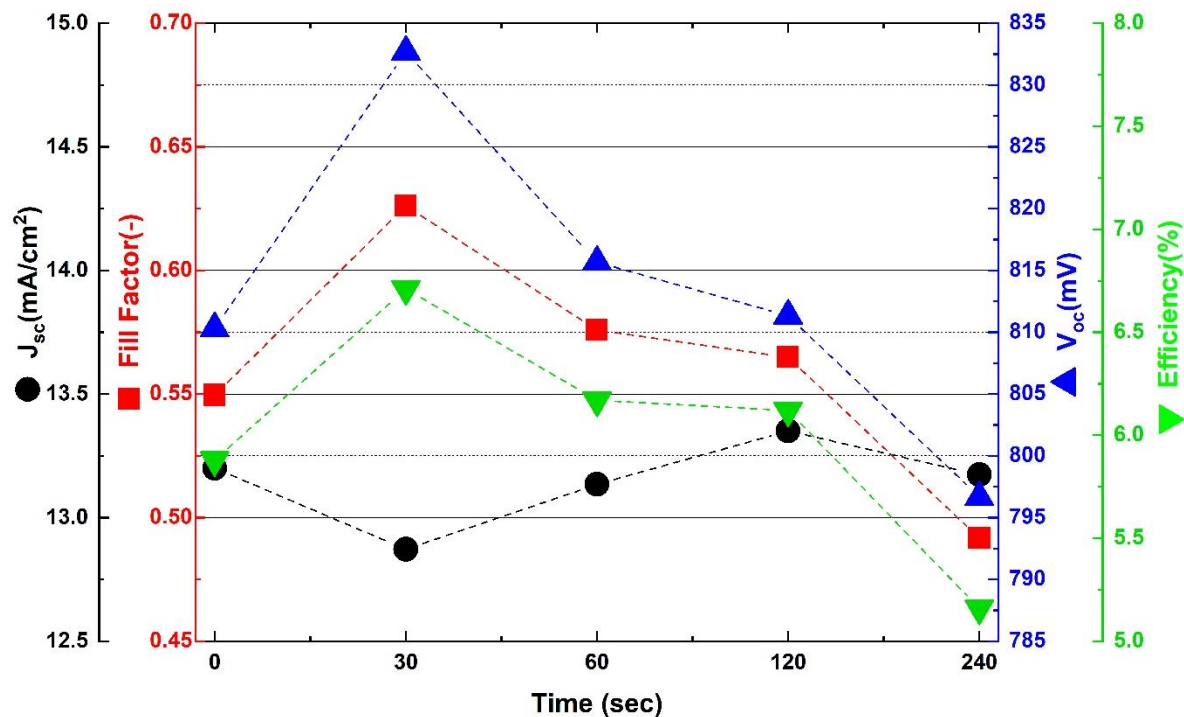
Figure 27 External parameters of solar cell as a function of time for post-HPT with a pressure of 1.2mBar and a power of 8W
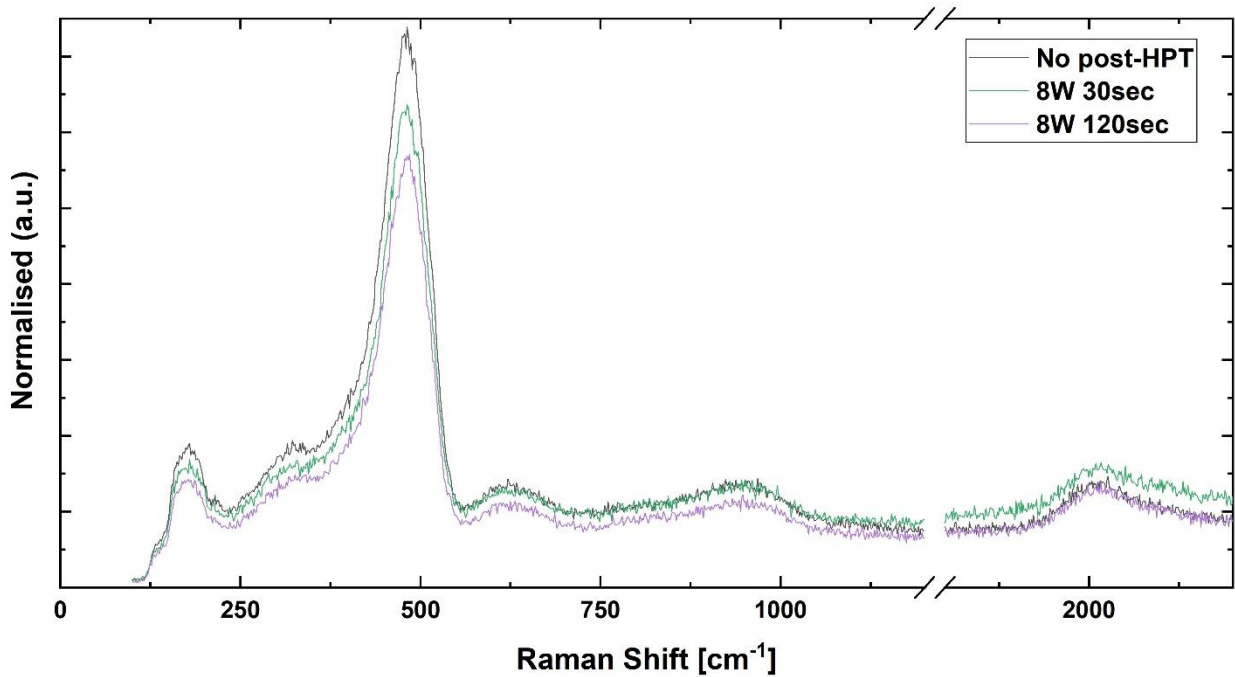
Figure 28: Raman spectroscopic analysis of post-HPT

In figure 28, it can be observed that there is decrease in the SiH bonds at the 2000 cm^{-1} wavenumber as the duration is increased. Also, a reduction in the intensity at the 480 cm-1 indicate that the quality of the layer is decreasing from amorphous to a more void rich material.

This chapter has dealt with the passivation of the i/p and p/ITO interface by HPT and hypothesised a possible reason for the ineffectiveness of the HPT at the i/p interface. The changes in the hydrogen ion concentration and energy due to the changes in plasma parameters affect the material at the surface and interstitial levels. The higher power HPT results in formation of more hydrogen ions in the plasma which can passivate the surface dangling bonds if the exposed duration is short. While higher pressure suppresses the HPT effect as the ions are colliding in the plasma instead of reacting with the substrate. The optimum power of 8W at 1.2 mBar of pressure for 30 seconds was found to give best result at the p/TCO interface. The open circuit voltage of the solar cell has been improved by 30mV with respect the reference *n-i-p* cell. The surface properties facilitate an optimum base for the deposition for the subsequent seed layer which will be discussed in the next chapter along with the effects of precursor gasses on p-nc-SiO$_x$ layer.

5. Optimization of p-Layer(s)

5.1 Introduction

The key purpose of the doped layers is to establish an internal electric field across the intrinsic layer for the separation of the charge carriers. This electric field directs the flow of generated charge carriers to their respective terminal contacts. The doped layers are not photo active layers, thus high transparency is important to limit the optical losses. To maximise the performance of a solar cell, maximum amount of incident light should reach the cell crossing through the p-layer. The generation of the electron hole pair adjacent to the p-layer helps in better collection of the holes since their drift lengths are much shorter compared to electrons. A high transverse conductivity of the window layer is required for a better FF and a high bandgap is required for a high built in voltage [24].

The mixed phase SiO_x has been known to fulfil the requirements of a good window layer. By varying the oxygen content, hydrogen dilution and the doping of this material, high transverse conductivity can be achieved even at higher bandgap energies. As mentioned, the mixed phase of SiO_x consists of a Si-rich phase and O-rich phase [25]. The high conductivity in SiO_x is due to the growth of crystalline filaments in the layer which are caused by the diffusion of silicon particles on the surface [26, 27].

In this study, a seed layer is deposited on the amorphous intrinsic layer to facilitate the growth of the crystalline filaments in the SiO_x layer, along with it the subsequent p-nc-SiO_x is optimised to be used as a window layer in a substrate configuration *n-i-p* solar cell.

5.2 Experimental Setup

The deposition of p-doped SiO_x is assisted by first preparing the absorber layer surface with uniformly distributed nano crystalline silicon seeds. This seed layer provides an anchor for the crystalline growth of the mixed phase SiO_x layer. The seed layer thickness optimization is carried out by varying the deposition time at a constant power of 35 W and pressure of 2.2 mBar. The silane (SiH_4) flow and hydrogen (H_2) flow were also kept constant at 0.8 sccm and 170 sccm respectively. During this series the thickness of the p-SiO_x layer is kept at 9nm, B_2H_6 of 20sccm, CO_2 of 2.3 sccm and H_2 of 170sccm.

With the cell schematics as described in the previous chapter, the boron doped silicon oxide layer is tuned by changing the B_2H_6, CO_2 and H_2 flow rates and the thickness of the layer to achieve a solar cell with high V_{oc} and FF parameters. Appropriate adjustments have been made to compensate for the changes in the deposition rate due to changes in the gas flow rates which has been reported in earlier research [28, 29].

Table 5.1: The deposition parameters for the seed layer and p-SiO$_x$.

Parameters	i-nc-Si:H	p-SiO$_x$:H
SiH$_4$ (sccm)	0.8	0.8
B$_2$H$_6$ (sccm) 200ppm in H$_2$	~	20-30
CO$_2$ (sccm)	~	1.8-2.8
H$_2$ (sccm)	170	170-200
Thickness (nm)	0-12	6-21

5.3 Results and Discussion

5.3.1 Effect of seed layer thickness

The effect of the thickness of the seed layer on external parameters of the solar cell are shown in figure 29. It is observed that the FF increases with increase in the seed layer but a maxima in V$_{oc}$ is reached at a thickness of 6nm. The increase in FF can likely be attributed to an increased transverse conductivity due to formation of large crystalline filaments.
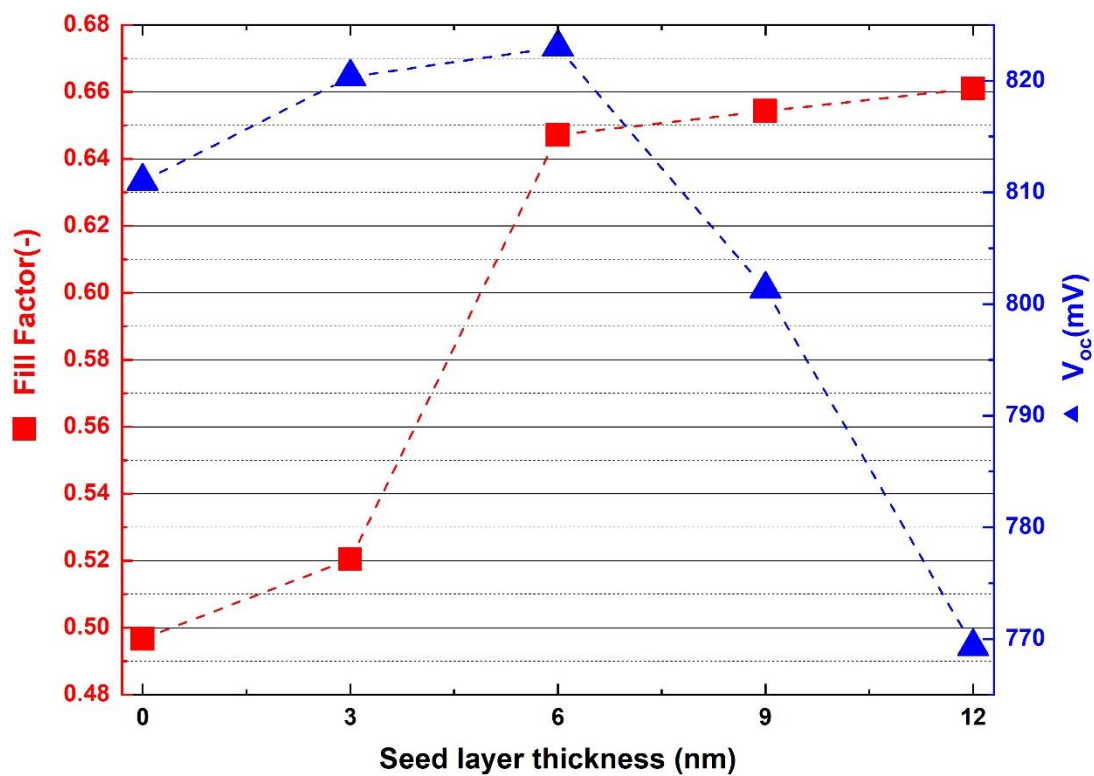
Figure 29: Solar cell parameters for the different thickness of the seed layer

This seed layer might affect the quasi fermi levels determining the built-in voltage i/p interface by two ways. Firstly, the bandgap of the i-layer is decreased because instead of i-a-Si the interface is now intrinsic nc-Si and secondly, at the interface there could be a change from p-a-SiO$_x$ to p-nc-SiO$_x$, lowering the bandgap of the p-layer. As the material is changing from amorphous to crystalline nature, the open circuit voltage decreases as seen in literature [30]. Taking 6nm of seed layer as a base value now the optimization of the p-nc-SiO$_x$ layer is carried out.

5.3.2 Effect of Precursor gases

<u>Diborane (B$_2$H$_6$), Carbon dioxide (CO$_2$) and Hydrogen (H$_2$)</u>

The effect of varying diborane and carbon dioxide in the p-SiO$_x$ layer on the solar cell parameters are shown in figure 30. It can be observed that the change in short circuit current is negligible throughout the range of CO$_2$. The Jsc is seen decreasing by 0.5 mA/cm^2 with the relative increase in diborane flow. It is likely a result of parasitic absorption since the increased doping decreases oxygenation in the material. But as the CO2 gas flow rate is increased to 2.8sccm the Jsc for all the diborane flow is levelized.
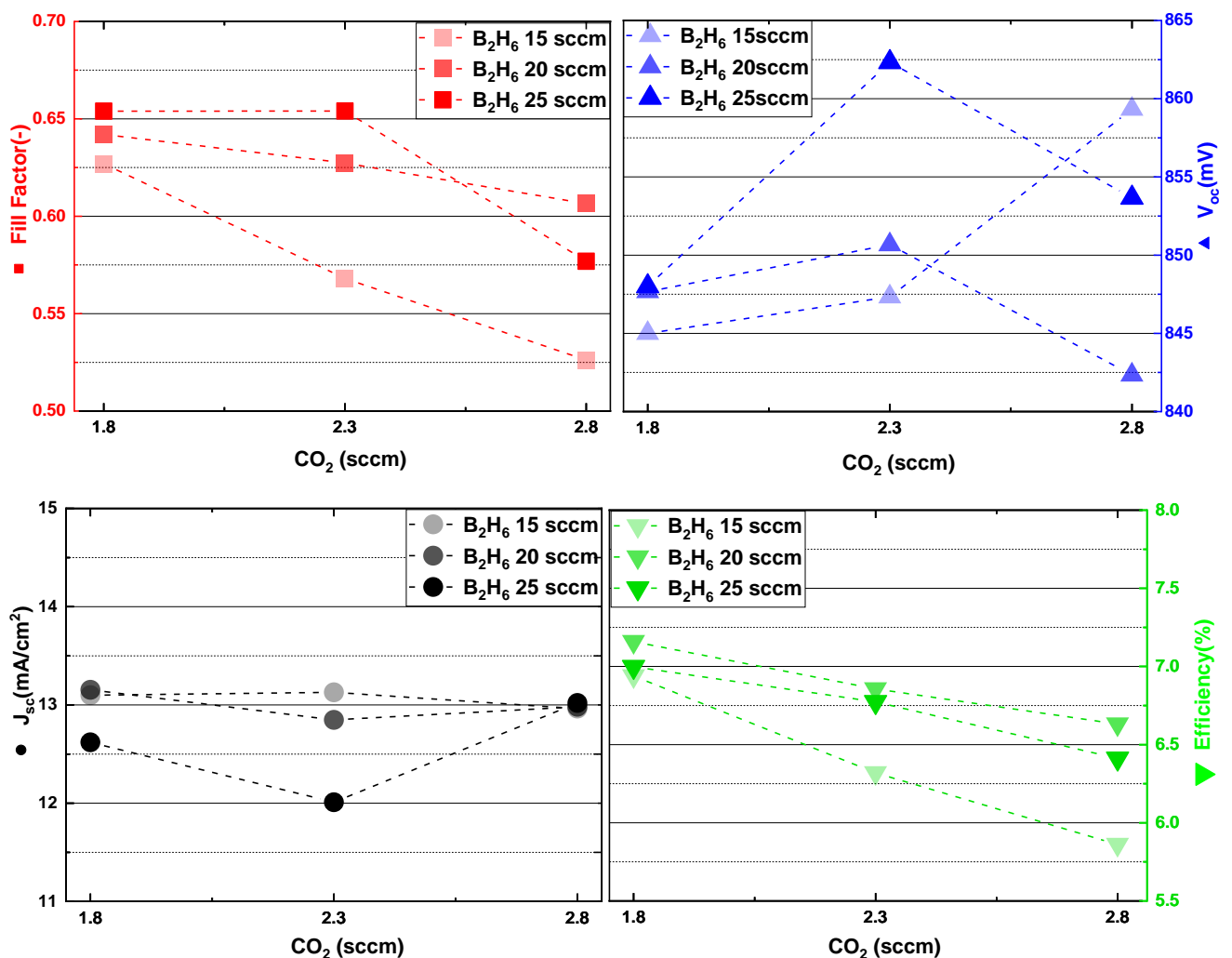
Figure 30: The solar cell parameters of cells with varying dopant and oxygen content in the window layer with hydrogen dilution at 170 sccm.

The increase in FF with increasing relative boron flow is more prevalent at higher relative CO_2 flow rates. A similar trend can be observed while comparing the V_{oc} of the cells. There is complex interplay in the material properties of SiO_x due to simultaneous changes in the flow rate of the precursor gases as it has been reported earlier [28, 29, 31-33]. The high relative flow of diborane results in the deposition of a more amorphous material which would indicate a higher optical bandgap. This may be due to the decrease in oxygenation of the material. This decrease in oxygen content also results in a more conductive film. With the aid of the nc-Si filaments, there is an increase in the lateral conductivity of the layer. This may lead to another possible effect where the more crystalline the film becomes the lower is the activation energy which in turn increases the conductivity. The increase in CO_2 flow rate has 2 effects: firstly, it increases the bandgap by increasing the number of SiO_x bonds and secondly a decrease in crystallinity since increased oxygenation suppresses the nucleation sites [24]. The higher diborane flow rate along with high CO_2 flow rate makes the layer more amorphous, thus reducing the conductivity of the layer.

*Figure 31: The solar cell parameters of cells with varying dopant and oxygen content in the window layer with hydrogen dilution at 200 sccm.*
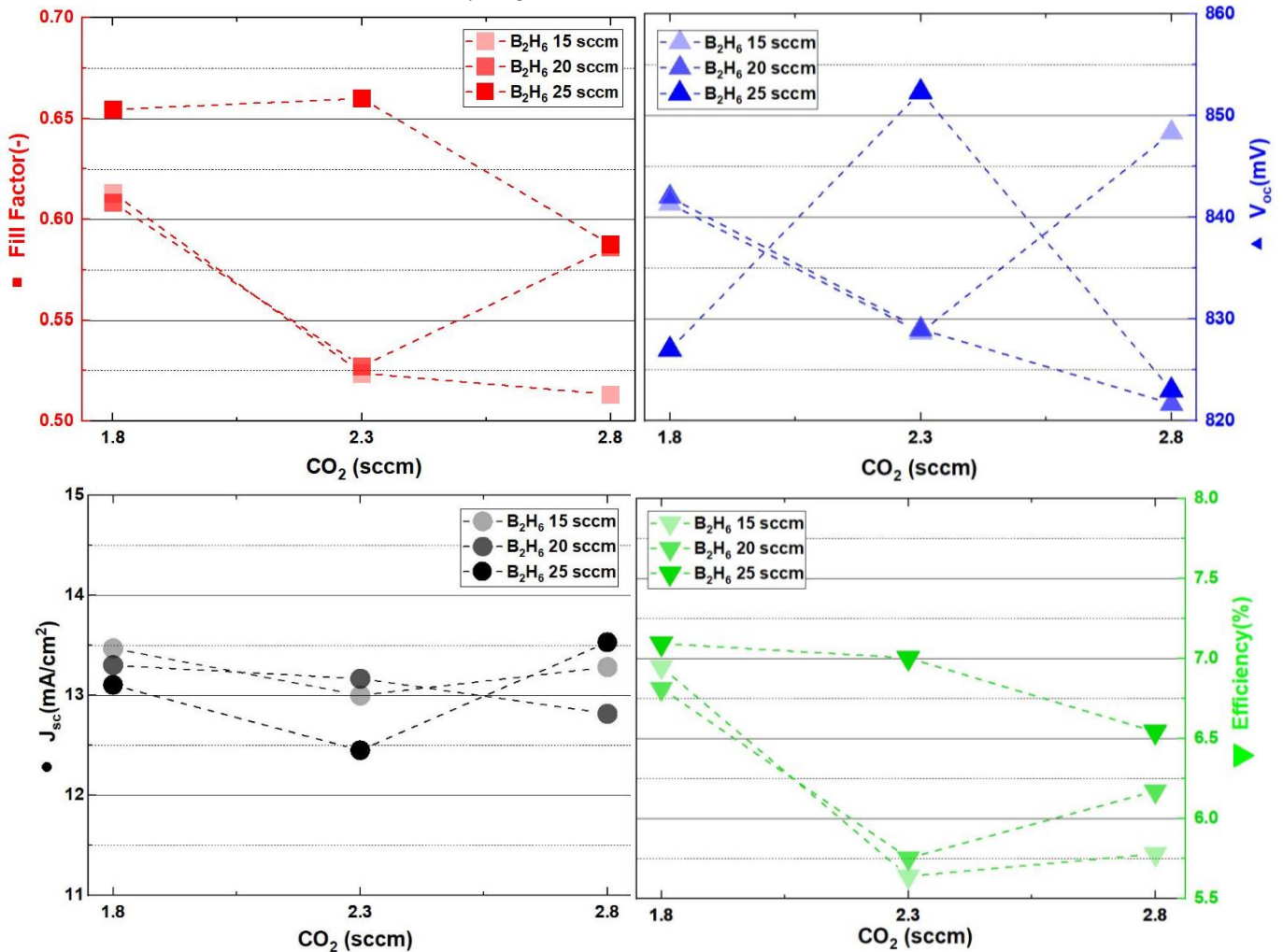
Figure 31 showcases similar trends as figure 30 with the difference of H_2 flow rate from 170 to 200sccm. Higher H_2 flow promotes crystallinity while also passivating the dangling bonds. This might result in formation of more nc-SiOx with lower bandgap than a-SiOx thus

decreasing the overall V_{oc} and increase in J_{sc} for the cells with B_2H_6 and CO_2 flow rates remaining identical to previous series.

5.3.3 Effect of thickness

With the precursor gas flow rate set for optimal performance and optimal material quality, the next step is to optimise the thickness of the p-SiOx layer. Figure 32 illustrates the parasitic absorption in the wavelength range from 300nm to 550nm which occurs by increasing the thickness of the window layer.
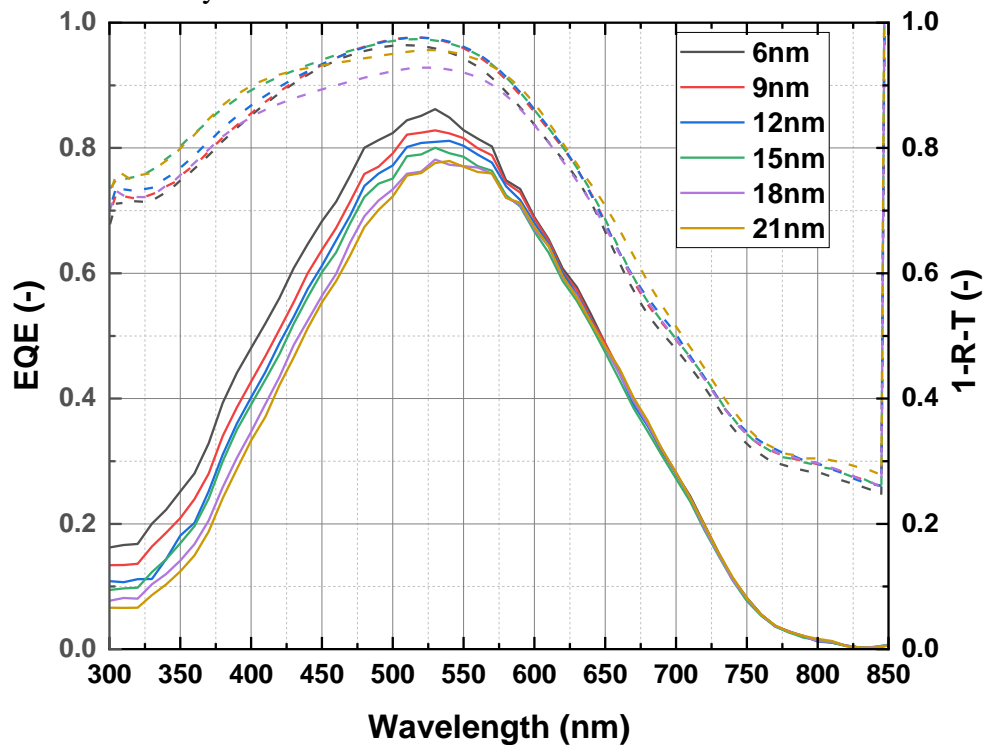
Figure 32: The EQE and absorptance curves for different thickness of p-SiO$_x$ layer with B$_2$H$_6$ at 25 sccm, CO$_2$ at 1.8sccm and H$_2$ at 170sccm flow rates.

The solar cell in this study has an absorber of thickness 250nm. Figure 33 showcases the external parameters of the solar cell for thickness varying from 6nm to 21 nm of the p-SiO$_x$ layer. The thinnest layer allows the charge carriers to pass through the layer to the external contact fairly easily thus giving high current density while at the same time it decreases the V_{oc} of the cell. The increase in thickness results in a gradual decrease in short circuit current. This can be attributed to a fact that the photogenerated holes takes longer time to reach the TCO than their mean lifetime. The thickness of p-layer is also dependent on the thickness of the i-layer. A minimum p-layer thickness ensures sufficient charge at the i/p interface to support the electric field for a given built in voltage [13]. Reducing the thickness below this minimum will result in a poorer V_{oc} of the cell while increasing it beyond a limit may result in high parasitic absorption.
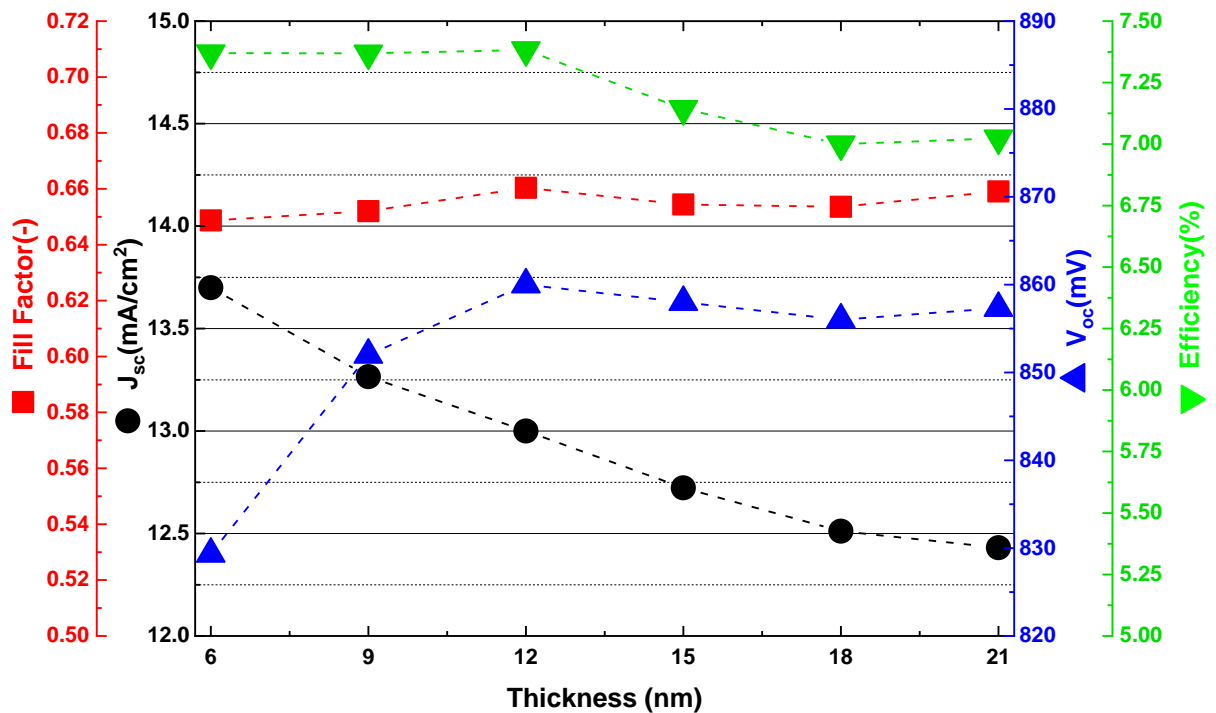
Figure 33: The solar cell parameters for varying thickness of the p-SiO$_x$ layer with B$_2$H$_6$ at 25 sccm, CO$_2$ at 1.8sccm and H$_2$ at 170sccm flow rates.

This chapter continued with the effects of the seed layer thickness an optimization of the seed layer thickness using the optimised HPT parameters. The i-nc-Si seed scattered on the i-a-Si laid a foundation for the growth of p-nc-SiO$_x$. With optimal thickness of 6nm, the seed layer provided optimum nano-crystalline grain size. Following the seed layer, the gas flow rates and thickness of the p-nc-SiO$_x$ layer are juggled to find the balance between the doping concentration, oxygenation and crystallinity of the layer while keeping the parasitic and reflection losses to a minimum. A high diborane flow results in high FF but also makes the material amorphous whereas a high H$_2$ flow increases the crystallinity of the material. A high CO$_2$ flow increases the optical SiOx bonds reducing the conductivity and transmittivity of the layer. The diborane flow of 25 sccm, CO$_2$ flow of 1.8 sccm and H$_2$ flow rate of 200 sccm gave a V$_{oc}$ of 848 mV, FF of 0.654, J$_{sc}$ of 12.6 mAcm^{-2} and an efficiency of 6.99%. With these optimized gas flow rates, the thickness of 12nm gave V$_{oc}$ of 860 mV, FF of 0.66, J$_{sc}$ of 13 mAcm^{-2} and an efficiency of 7.38%. With these conditions, the next chapter aims deals with the thickness optimization of the contact layer and the TCO layer.

6. Contact layer and TCO

6.1 Introduction

The properties of a contact layer at the p/TCO interface play an important role in determining the performance of the cell by improving the carrier recombination of electron with holes in the external circuit and series resistance. An intermediate layer can help in band alignment between the different bandgap levels of the p-layer and the TCO. Being the first medium of interaction for the incident light, the TCO and the contact layer should be transparent and have a high band gap to reduce any parasitic absorption. In this section the thickness of the remaining segments of the window layer are investigated an optimized for the a-Si solar cell.

6.2 Experimental setup

A series of varying thickness of Indium Tin oxide (ITO) is carried out with the optimised parameters of previous chapters and keeping the p-nc-Si contact layer at a thickness of 5nm with the diluted diborane flow of 30 sccm.

The subsequent series for comparison of the contact layer between p/TCO interface is fabricated with a varying boron doping and thickness. The HPT on this contact layer is kept constant at power of 8W, pressure of 1.2 mBar and time of 30seconds. The precursor gas flow rates are listed in table 6.1 along with the thickness of the p-nc-Si. The TCO used in here is 75nm of ITO which is sputtered in a separate cluster tool called Zorro.

Table 6.1: The deposition parameters for the doped contact layer at the p/TCO interface.

Parameters	p-nc-Si:H
SiH_4 (sccm)	0.8
B_2H_6 (sccm) 200ppm in H_2	30
CO_2 (sccm)	~
H_2 (sccm)	170
Power (W)	35
Pressure (mBar)	2.2
Heater Temperature (°C)	300
Thickness (nm)	0-12

6.3 Results and discussion

6.3.1 Effect of TCO thickness

On analysing the external solar cell parameters in figure 34, it can be said that the thickness range of the ITO from 60 – 85 nm does not affect the open circuit voltage of the cell by more than ±5mV. While a steady drop in the short circuit current density is notable. This drop can be attributed to the reflection losses which is clearly visible in the EQE and absorption curves in figure 35 from wavelength 300-550 nm. The deflections in the FF may be within the processing error margin. The increase in thickness of the ITO improves the electrical properties of the layer but deteriorates the optical properties. The optical transmittance decreases with the increase in ITO thickness as the incident light is reflected. To keep the losses to a minimum the ITO thickness is fixed at 60nm to maintain optimum electrical and optical properties for the next series.
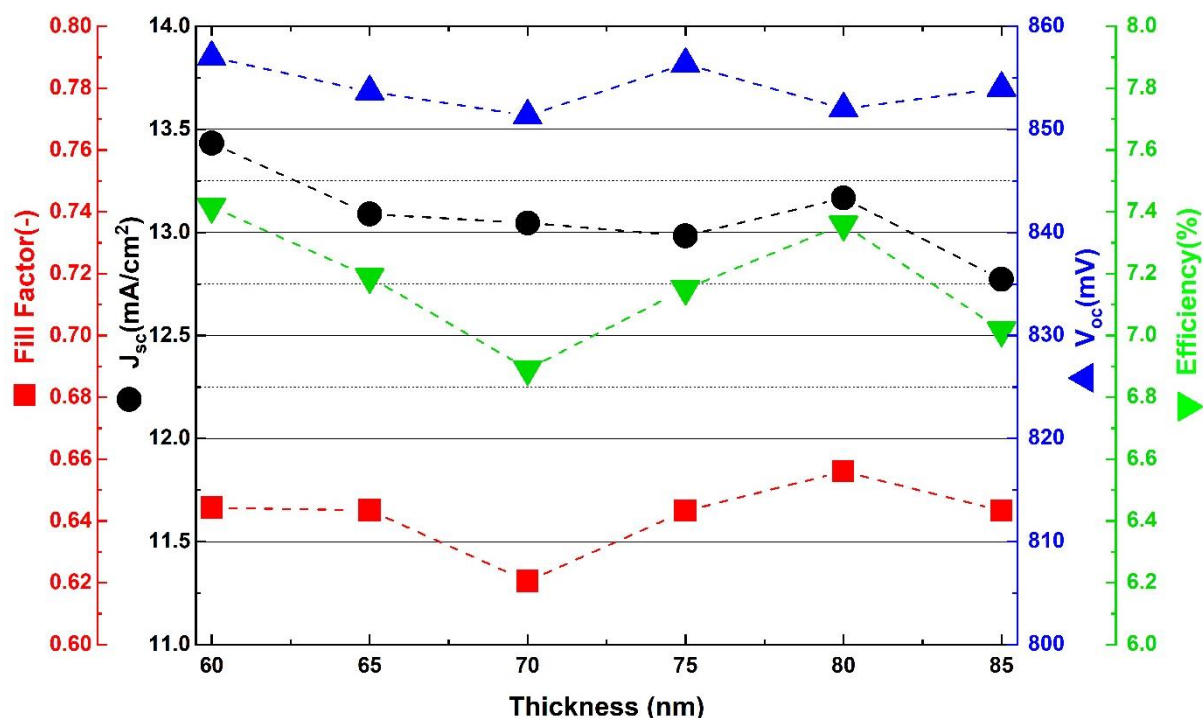
Figure 34: The solar cell parameters for different thickness of ITO

6.3.2 Effect of contact layer thickness

The presence of a contact layer may facilitate collection of charge carriers by improving the band alignment, but it also risks becoming one of the factors contributing to spectral losses. In the EQE plot (figure 36) of the series, this effect can be visualised. The parasitic losses occurring in the wavelength range of 300-550nm with increasing thickness of the contact layer does not contribute to the photo generated charge carrier. In figure 37 two opposite trends can be observed: increase in FF and V_{oc} and decrease in J_{sc}. The decrease in series resistance likely improves the band alignment which results in the improvement of the FF with the thickness of the layer. Improved surface passivation due to post HPT may also be one of the reasons for the
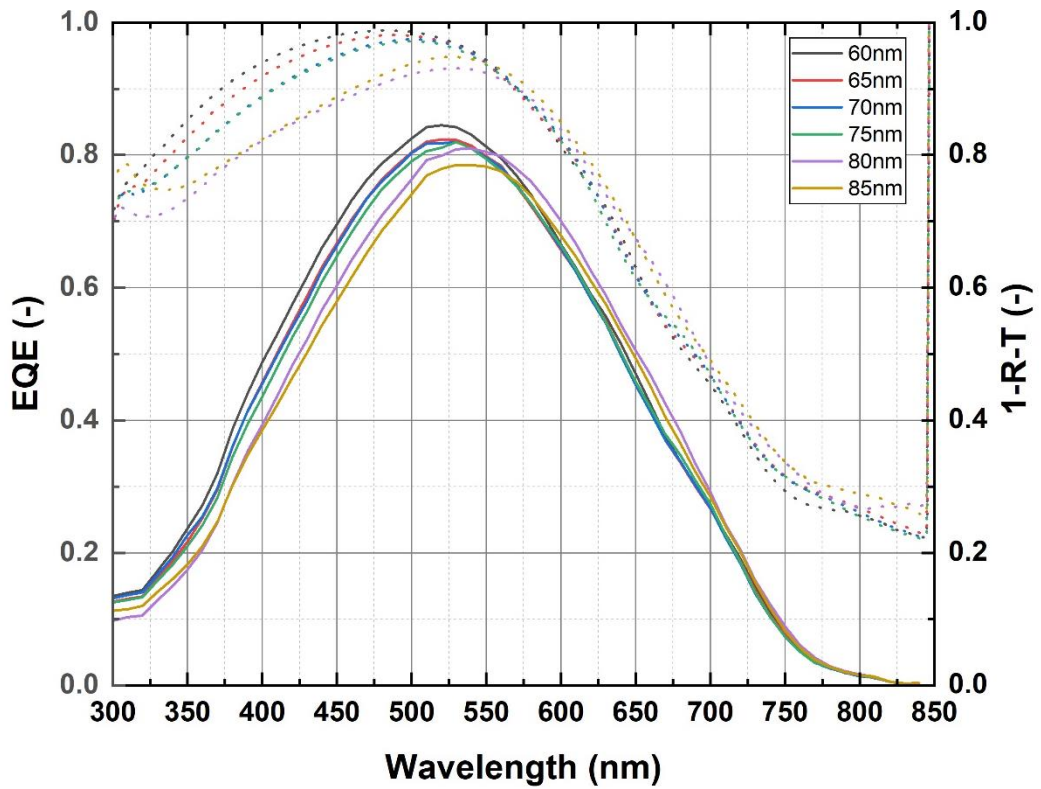
Figure 35: The EQE and absorption curve for different thickness of ITO

increase in the FF. The 60mV increase in V_{oc} due to the addition of the p-nc-Si as a contact layer can be attributed to the improved transfer of charge carriers at the p/ITO interface. The reduced number of photons reaching the active region results in the decrease in J_{sc} with increasing thickness.
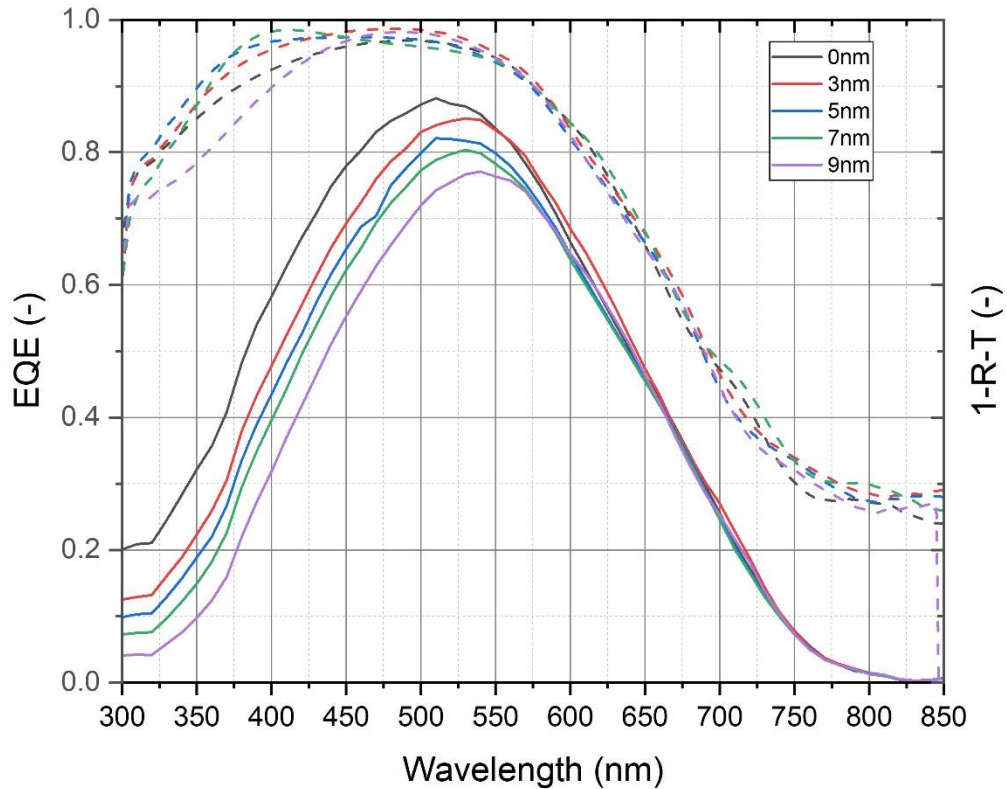
Figure 36: The EQE and absorption curve for different thickness of contact layer
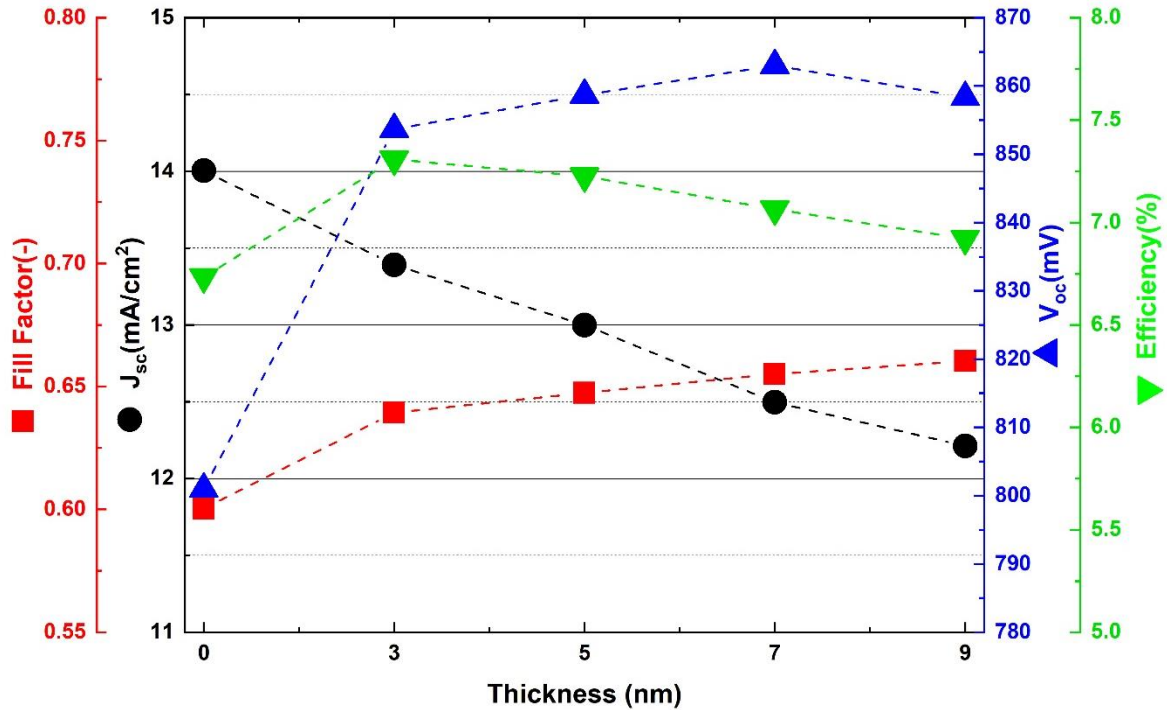
Figure 37: The solar cell parameters for different thickness of contact layer

To minimize the parasitic and reflection losses the thickness the ITO and the contact layer between the ITO/p-layer interface are optimised. The thickness of the ITO is varied from 60nm to 85 nm in steps of 5nm. The EQE for this series shows the textbook curves of the effect of parasitic absorption. The minimum thickness of 60 nm has been fixed to maintain the relative transverse conductivity of the layer. The contact layer is a p-nc-Si layer doped with a higher diborane flow of 30 sccm compared to the p-nc-SiO$_x$ layer. A thickness of 3 nm of contact layer shows a tremendous performance boost in terms of the V$_{oc}$ of the cell from 800mV to 855 mV. Constant decrease in the J$_{sc}$ and increase in the FF are due to the decrease in series resistance. Even though the FF and V$_{oc}$ reaches maximum value at 7nm thickness, but the 3nm thick contact layer is considered as an optimised value due to the lowest parasitic losses. At a thickness of 3 nm the J$_{sc}$ is 13.5mAcm^{-2} which gives room for adjusting the thickness of the absorber layer in upcoming multi-junction device for a better current matching.

7. Multi-junction solar cell

7.1 Introduction

The optimization of the HPT, properties and thickness of the window layer and the TCO layer are now implemented in the fabrication of a 2-junction solar cell. The top cell is a high bandgap hydrogenated amorphous silicon while the bottom cell is hydrogenated silicon germanium alloy for improved band gap utilization. The following series of multi-junction solar cells are preliminary test cells to make a current matched device by varying the absorber thickness of the top and bottom cell and grading of the bottom cell. This work is initially simulated using a matlab software called Genpro4.

7.2 Experimental setup

The fabrication of the multi junction solar cell was performed in EKL lab. The cell schematics is as follows: Asahi Glass/ FTO/ protective AZO/ n-nc-Si/ n-nc-SiOx/ n-nc-SiOx/ n-a-Si/HPT/ /i-a-SiGe:H/HPT/ i-nc-Si (seed layer)/ p-nc-SiOx/ p-nc-Si/HPT/ n-nc-Si/ n-a-Si/ i-a-Si:H/ i-nc-Si (seed layer)/ p-nc-SiOx/ p-nc-Si/HPT/ ITO/ metal grid.

Table 7.1: The changes in the parameters of the two absorber layers.

Parameters	i-a-SiGe:H	i-a-Si:H(High)	i-a-Si(Low)
SiH$_4$ (sccm)	30	2	40
GeH4 (peak)	5.3	~	~
H$_2$ (sccm)	200	200	~
Bandgap shape	V-U	~	~
Power (W)	3	9	2.8
Pressure (mBar)	3.6	10	0.7
Heater Temperature (°C)	300	200	300
Thickness (nm)	170	150-200-250	250

Initially a comparison of a low bandgap and high bandgap top cell is performed followed by the changes as described in table 7.1. The External parameters of the tandem cell were measured as described in the previous chapters with the exception of EQE. The EQE of each cell in the tandem is measured by flooding the other cell with appropriate bias light. The figure 38 shows the spectral photon flux density of all the bias LED lights available in the EQE setup. To measure the J_{sc} of the top cell, the bottom cell is flooded with bias lights of peak wavelength of 850 nm and 935 nm. Similarly, to measure the J_{sc} of the bottom cell, the top cell is flooded with bias lights of wavelength 365nm, 400 nm and 447.5 nm.

A V-shape bandgap refers to the increasing flow rate of GeH4 from 0sccm to a peak value till a specific width of the absorber layer and then immediately decreasing it back to 0. A U-Shape bandgap is similarly prepared with the exception that the peak flow rate is maintained for a almost 33% of the total width of the absorber layer. The peak flow rate of Ge to fabricate a V-shape and U shape bandgap is 5.3 sccm. While performing the simulations, the SiGe layer was assumed to have a uniform germanium deposition without and bandgap shaping. To compensate for this, the n-k data used is of a SiGe layer with the average flow rate of Ge. For the V-shape, assuming a lower concentration of Ge, a uniform deposition with GeH4 flow rate of 3.3sccm is considered and for the U-shape a flow rate of 4.3 sccm is taken.
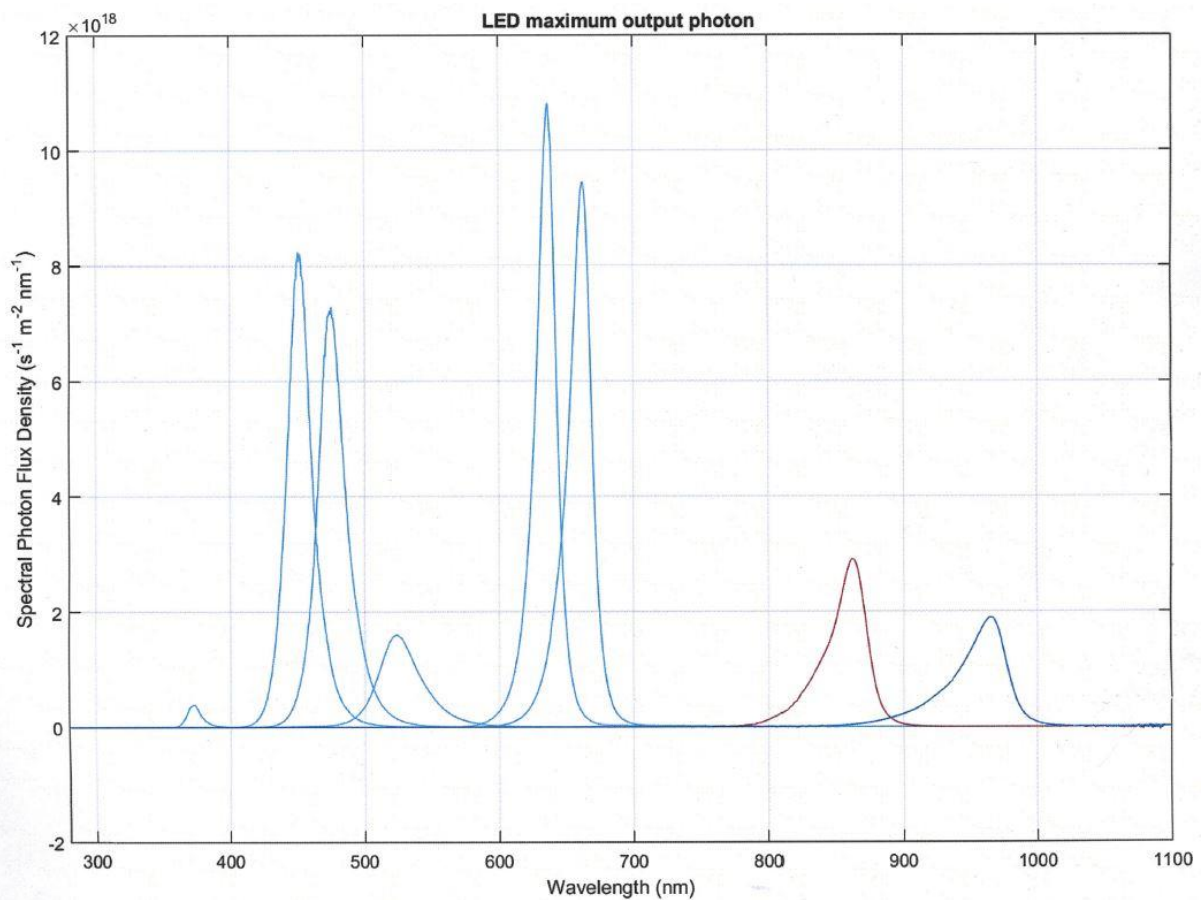

Figure 38: The Spectral photon flux density of the bias lights available in the EQE setup

7.3 Results and discussion

7.3.1 Comparison of a-Si (Low) and a-Si:H (High) in tandem

The low bandgap a-Si as top cell and the best performing a-SiGe:H as bottom cell show a large current mismatch of 5.71 mAcm^{-2}. The bottom cell acts as the current limiting cell in this configuration. The low bandgap a-Si is replaced with a high bandgap a-Si:H to improve the spectral utilization. The bottom cell is still current limiting but the difference in current density has been reduced 2.56 mAcm^{-2}. The FF increases from 0.66 to 0.69. An increase in the open circuit voltage by 40 mV is also observed which is due to the use of high bandgap a-Si:H. The increase in FF can be attributed to the decrease in the series resistance from 21.0Ωm^2 to 14.9Ωm^2. A speculation that he presence of hydrogen ions in the plasma contributed to the passivation of the dangling bonds in the absorber layer resulting in better performance than the low bandgap a-Si or the band alignment at the interface.
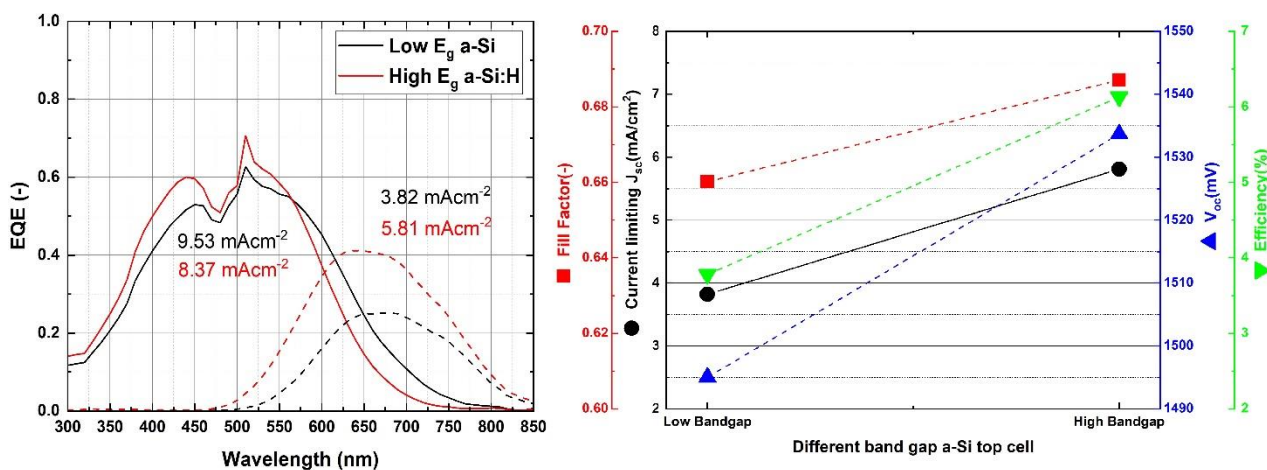
Figure 38: EQE and Solar cell parameters of tandem cells with a-Si (Low) and a-Si:H (High)

7.3.2 Tandem with V-Shape bandgap of bottom cell

To make a current matched 2-junction device, the thickness of the top cell is varied while keeping a constant thickness for the V-shaped bandgap bottom cell at 170nm. It is observed that for a top cell thickness of 200 nm the difference in current density is reduced to just 0.229 mAcm^{-2} with the top cell acting as the current limiting cell. The increase in thickness usually results in lower V$_{oc}$, FF and efficiency but an increase in the FF is noted which may be due to the increased current mismatch in the device.

The EQE in the figure 39 shows a lower J$_{sc}$ for the thin 150 nm top cell at 5.71mAcm^{-2} whereas the expected J$_{sc}$ is around 7.5 mAcm^{-2}. This may be due to the non-uniform deposition of the layer. The receding EQE curve from the 400nm to 450 nm wavelength also indicates a increased absorption in the top cell.
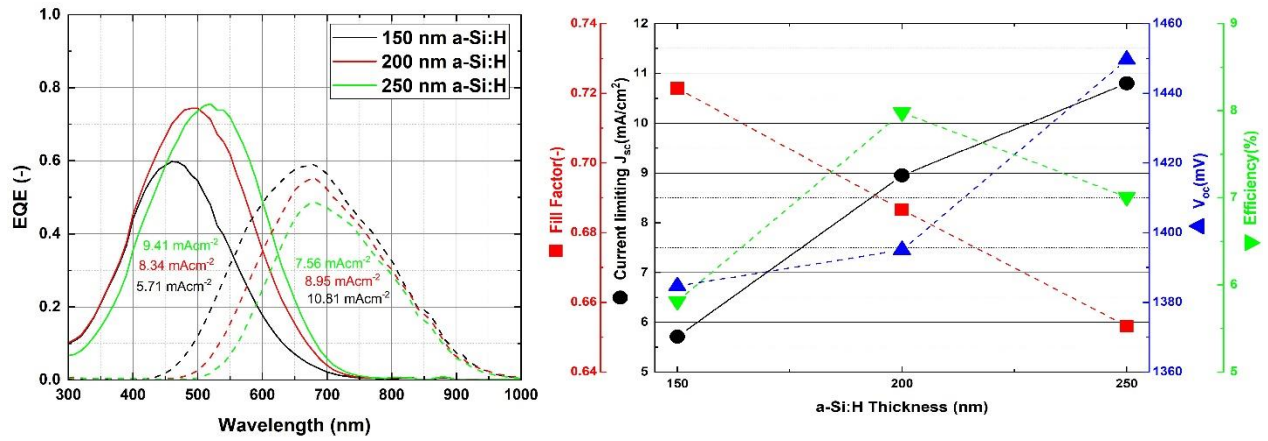
Figure 39: EQE and Solar cell parameters of tandem cells with varying thickness of a-Si:H (High) for V shape bottom cell.

Table 7.2: The external solar cell parameters with 170 nm of V shaped i-SiGe:H

	Tandem 1	Tandem 2	Tandem 3
a-Si Thickness (nm)	150	200	250
V_{oc} (mV)	1385	1395	1397
FF (-)	0.72	0.69	0.67
J_{sc} Top (mAcm^{-2})	5.71	8.34	9.14
J_{sc} Bottom (mAcm^{-2})	7.56	8.95	10.81
Efficiency (%)	5.81	7.99	7.06

7.3.3 Tandem with U-shape bandgap bottom cell

The effect of U-shape bandgap for the bottom a-SiGe:H cell is observed on the varying thickness of the top a-Si:H cell. An opposite trend is noted with respect to the V-shape in the previous section. The V_{oc} and FF both are decreasing with increase in thickness. It can be speculated that the U-shape has an increased concentration of germanium in the layer which reduces the bandgap and in turn reduces the V_{oc}, while the increase in the series resistance may contribute to the decrease in the FF of the tandem cell.

The EQE of the tandem cells in figure 40 shows that the top cell is the current limiting cell in all the cases. This can be attributed to the high germanium content of the U shape bottom cell which has a lower bandgap than the V shape thus resulting in more absorption of light.
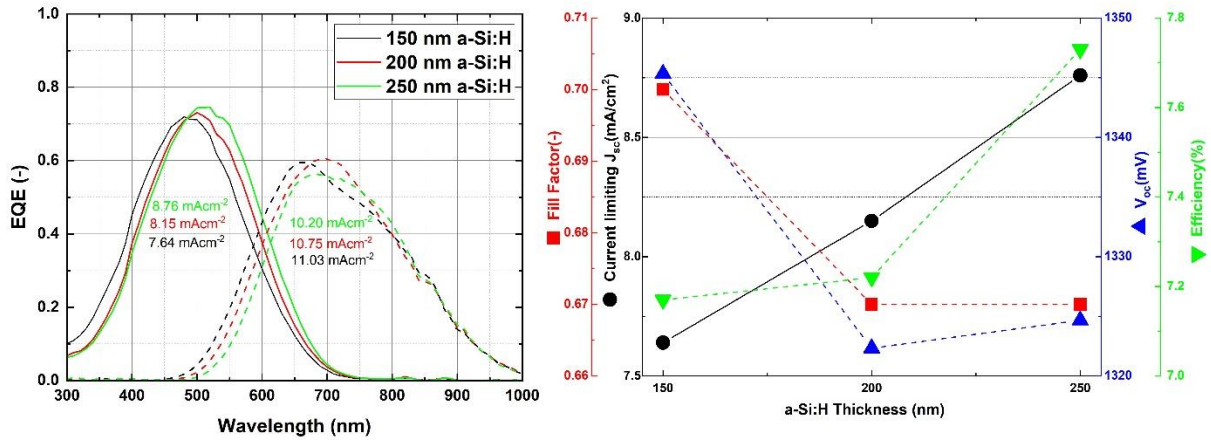
Figure 40: EQE and Solar cell parameters of tandem cells with varying thickness of a-Si:H (High) for U shape bottom cell.

Table 7.3: The external solar cell parameters with 170 nm of U shaped i-SiGe:H

	Tandem 4	Tandem 5	Tandem 6
a-Si Thickness (nm)	150	200	250
V_{oc} (mV)	1345	1322	1325
FF (-)	0.69	0.67	0.66
J_{sc} Top (mAcm^{-2})	7.64	8.15	8.76
J_{sc} Bottom (mAcm^{-2})	11.03	10.75	10.20
Efficiency (%)	7.17	7.22	7.73

The difference in low bandgap a-Si and high bandgap a-Si:H reflects in the performance boost by an increase in V_{oc} of 40 mV and in FF from 0.66 to 0.672 but due to the current mismatch the overall performance is degraded and J_{sc} is limited to 5.81 mAcm^{-2}. A high potential multi-junction device fabricated with a 200nm high bandgap a-Si:H and a 170nm low V-shaped bandgap a-SiGe:H generates a V_{oc} of 1395 mV, a FF of 0.69, efficiency of 7.99% and a current limited top cell with J_{sc} of 8.34 mAcm^{-2}. The difference in the J_{sc} for this tandem is only 0.61mAcm^{-2}. These preliminary results are promising since the cell has no dedicated tunnel recombination junction or a metal back reflector.

8. Conclusion

The main objective of this work was to optimise the window layers of a *n-i-p* configured a-Si solar cell to maximize the V_{oc} and FF for use as a top cell in a multi-junction device. This multi-junction device can be used for applications such as water splitting, water cleaning and CO2 reduction, which are all potential dependent processes. With this as a motivation a series of optimizations were carried out. Initially various configurations of hydrogen plasma treatment were investigated at the i/p interface and p/TCO interface. This was followed by improving the thickness of the seed layer and optimizing the precursor gas flow rates and thickness of the p-doped mixed phase silicon oxide layer. Next the contact layer and the TCO thickness were tweaked for maximum performance. Lastly, a 2-junction tandem was fabricated and current matched for a achieving a high potential solar cell.

The HPT effects were observed at varying power and pressure settings along with the time of exposure. It was observed that the power and pressure series of pre-HPT and post HPT when performed do not show conclusive results. Thus, a mini-series of the pre-HPT, post-HPT and pre-post HPT showcases that the effect of post-HPT and pre-post HPT give V_{oc} with 815 mV and 809 mV and the change in FF is 0.05%. This undermining of the pre-HPT can be attributed to the fact that plasma formed during the deposition of the seed layer before the p-layer contains hydrogen ions and radicals in considerable concentrations. This may partially act as HPT alongside the deposition of nano-crystalline silicon seed layer. The optimised post-HPT parameters of 8W power, 1.2 mBar of pressure and 30 seconds of exposure time boosts the V_{oc} from 810 mV to 832mV and the FF from 0.55 to 0.625. Longer duration of HPT may result in ion bombardment and destruction of the material reducing its performance.

Since the absorber is amorphous in nature, the growth of p-nc-SiO$_x$ is facilitated by planting some "seeds" of i-nc-Si. This layer forms a base for the development of crystalline filaments, and it can be speculated that their thickness determines the crystallinity of the p-layer. The influence of the precursor gas flow on the material, electrical and optical properties of the p-SiO$_x$ layer was analysed. A thickness of 6nm of the seed layer increases the V_{oc} from 810mV to 822mV and the increase in FF is from 0.55 to 0.65. A thicker seed layer may not be optimum for the growth of nano-crystalline SiO$_x$ layer. A higher dopant flow and lower oxygen in the plasma have resulted in a layer which is highly transparent and conductive. The diborane flow of 25 sccm, CO$_2$ flow of 1.8 sccm and H$_2$ flow rate of 200 sccm gave a V_{oc} of 848 mV, FF of 0.654, J$_{sc}$ of 12.6 mAcm^{-2} and an efficiency of 6.99%. With these optimized gas flow rates, the thickness of 12nm gave V_{oc} of 860 mV, FF of 0.66, J$_{sc}$ of 13 mAcm^{-2} and an efficiency of 7.38%.

The thickness of the last two segments of the window layer including the ITO are optimised to ease the bandgap alignment at the ITO-semiconductor junction and to minimize the parasitic absorption losses. The ITO thickness of 60nm showcases low reflection and parasitic losses while maintaining the electrical properties. The contact layer thickness of 3nm is considered

optimum in this work since it significantly increases the V_{oc} and FF while keeping the parasitic losses to the minimum. The resulting cell has an increased FF from 0.60 to 0.65 while the V_{oc} has increased from 800mV to 855mV. The J_{sc} of 13.5mAm_{-2} at 3nm thickness is observed to be decreasing with increasing contact layer thickness but since the current through the multijunction device is limited by the cell with minimum J_{sc}, the a-Si cells fabricated have a leeway in the absorber layer thickness for current matching in a tandem cell.

With the window layer optimised for the top cell, a tandem cell is fabricated with 170 nm V-shaped bandgap a-SiGe:H and a high bandgap a-Si:H. For current matching bot the cells, the thickness of the top cell is decreased and 200nm is observed to have minimum J_{sc} difference of 0.61mAcm^{-2} while the V_{oc} is 1395 mV, FF is 0.69 and efficiency of 7.99%.

Further research in the tunnel recombination junction and the use of other absorber materials like c-Si and a-GeSn to form a quadruple junction is highly interesting.

Bibliography

[1]   H. Ritchie and M. Roser. "Energy Production & Changing Energy Sources." https://ourworldindata.org/energy-production-and-changing-energy-sources (accessed.

[2]   H. Ritchie and M. Roser. "CO₂ and Greenhouse Gas Emissions." https://ourworldindata.org/co2-and-other-greenhouse-gas-emissions (accessed.

[3]   I. Fodriest Environmental. "Solar Radiation and Photosynethically Active Radiation." https://www.fondriest.com/environmental-measurements/parameters/weather/solar-radiation/ (accessed.

[4]   *IEC 60904-3,Photovoltaic devices – Part 3: Measurement principles for terrestrial photovoltaic (PV) solar devices with reference spectral irradiance data*, I. E. Commission, 2008.

[5]   R. Nave. "Band Theory for Solids." http://hyperphysics.phy-astr.gsu.edu/hbase/Solids/band.html (accessed 31/08/2019.

[6]   W. Shockley and H. J. Queisser, "Detailed Balance Limit of Efficiency of p-n Junction Solar Cells," *Journal of Applied Physics,* vol. 32, pp. 510-519, March 01, 1961 1961. [Online]. Available: https://ui.adsabs.harvard.edu/abs/1961JAP....32..510S.

[7]   A. H. M. Smets, K. Jäger, O. Isabella, R. A. v. Swaaij, and M. Zeman, *Solar energy : the physics and engineering of photovoltaic conversion, technologies and systems*. Cambridge, England :: UIT Cambridge Ltd. (in English), 2016.

[8]   P. P. Rodriguez, "Photovoltaic-(photo)electrochemical devices for water splitting and water treatment," PhD, Technische Universiteit Delf, 2018.

[9]   Z. Yu, I. Pereyra, and M. N. P. Carreno, "Wide optical band gap window layers for solar cells," *Solar Energy Materials and Solar Cells,* vol. 66, no. 1, pp. 155-162, 2001/02/01/ 2001, doi: https://doi.org/10.1016/S0927-0248(00)00168-9.

[10]   K. L. Chopra, P. D. Paulson, and V. Dutta, "Thin-film solar cells: an overview," *Progress in Photovoltaics: Research and Applications,* vol. 12, no. 2-3, pp. 69-92, 2004, doi: 10.1002/pip.541.

[11]   M. Vaqueiro-Contreras *et al.*, "Identification of the mechanism responsible for the boron oxygen light induced degradation in silicon photovoltaic cells," *Journal of Applied Physics,* vol. 125, no. 18, p. 185704, 2019, doi: 10.1063/1.5091759.

[12]   T. d. Vrijer, "Stability and Performance of Doped Silicon Oxide Layers for Use in Thin Film Silicon Solar Cells," M.Sc. in Sustainable Energy Technology, Delft University of Technology, 2015.

[13]   C. Ballif, W. Beyer, F. Finger, H. Schade, A. Shah, and N. Wyrsch, A. Shah, Ed. *Thin Film Silicon Solar Cells*. EPFL Press, 2010.

[14]   G. Horowitz, "Validity of the concept of band edge in organic semiconductors," *Journal of Applied Physics,* vol. 118, p. 115502, 09/21 2015, doi: 10.1063/1.4931061.

[15]   G. Yang, "High-efficient n-i-p thin-film silicon solar cells," Ph.D., Delft University of Technology, 2015.

[16]   X. Ma. and W.-H. Huang. "Introduction to I-V curves." https://cran.r-project.org/web/packages/ddiv/vignettes/IVcurve.html (accessed.

[17]   A. Rosenberg, D. Hu, H. Chouaib, Z. Tan, and N. Malkova, *Tracking the defects and the band gap of ultra-thin HfO2 using a multi-oscillator Cody Lorentz model*. 2018, p. 102.

[18]   H. Sakai, T. Yoshida, S. Fujikake, T. Hama, and Y. Ichikawa, "Effect of p/i interface layer on dark J-V characteristics and Voc in p-i-n a-Si solar cells," *Journal of Applied Physics,* vol. 67, no. 7, pp. 3494-3499, 1990, doi: 10.1063/1.345340.

[19] J. Wang, K. Tao, H. Cai, D. Zhang, and G. Li, "A study of the i/p interface for flexible n–i–p a-Si:H thin film solar cells," *Materials Science in Semiconductor Processing,* vol. 25, pp. 186-189, 2014/09/01/ 2014, doi: https://doi.org/10.1016/j.mssp.2013.11.024.

[20] A. Sturiale and F. A. Rubinelli, "Evidences of the defect pool model in the dark current-voltage characteristics of hydrogenated amorphous silicon based p-i-n devices," *Thin Solid Films,* vol. 516, no. 21, pp. 7708-7714, 2008/09/01/ 2008, doi: https://doi.org/10.1016/j.tsf.2008.04.002.

[21] J. Perrin, P. R. i. Cabarrocas, B. Allain, and J.-M. Friedt, "a-Si:H Deposition from SiH4and Si2H6rf-Discharges: Pressure and Temperature Dependence of Film Growth in Relation to α-γ Discharge Transition," *Japanese Journal of Applied Physics,* vol. 27, no. Part 1, No. 11, pp. 2041-2052, 1988/11/20 1988, doi: 10.1143/jjap.27.2041.

[22] J. Perrin, "Plasma and surface reactions during a-Si:H film growth," *Journal of Non-Crystalline Solids,* vol. 137-138, pp. 639-644, 1991/01/01/ 1991, doi: https://doi.org/10.1016/S0022-3093(05)80202-9.

[23] C.-F. Chen and Y.-W. Li, "The Effects of Hydrogen Plasma Treatment on the Plasma-Enhanced Chemical Vapor Deposition a-SiC:H Films," *Japanese Journal of Applied Physics,* vol. 43, no. 8A, pp. 5545-5549, 2004/08/10 2004, doi: 10.1143/jjap.43.5545.

[24] H. Tan, P. Babal, M. Zeman, and A. H. M. Smets, "Wide bandgap p-type nanocrystalline silicon oxide as window layer for high performance thin-film silicon multi-junction solar cells," *Solar Energy Materials and Solar Cells,* vol. 132, pp. 597-605, 2015/01/01/ 2015, doi: https://doi.org/10.1016/j.solmat.2014.10.020.

[25] R. Biron, C. Pahud, F.-J. Haug, J. Escarré, K. Söderström, and C. Ballif, "Window layer with p doped silicon oxide for high Voc thin-film silicon n-i-p solar cells," *Journal of Applied Physics,* vol. 110, no. 12, p. 124511, 2011, doi: 10.1063/1.3669389.

[26] H. L. P. Babal, L. Xie, B. van Veen, M. van Sebille, H. Tan, M. Zeman, A. Smets, "Nanostructure Analysis of P-Doped Nanocrystalline Silicon Oxide," presented at the 28th European Photovoltaic Solar Energy Conference and Exhibition, 2013.

[27] P. Cuony *et al.*, "Silicon Filaments in Silicon Oxide for Next-Generation Photovoltaics," *Advanced Materials,* vol. 24, no. 9, pp. 1182-1186, 2012, doi: 10.1002/adma.201104578.

[28] C. B. Singh, S. Bhattacharya, N. Ahmed, and P. B. Bhargav, "Effect of boron doping on optical and electrical properties of p-type a-Si:H films for thin film solar cells application," in *2014 1st International Conference on Non Conventional Energy (ICONCE 2014)*, 16-17 Jan. 2014 2014, pp. 38-42, doi: 10.1109/ICONCE.2014.6808678.

[29] T. d. Vrijer. and A. Smets., "Sensitivity of the opto-electrical properties of doped silicon layers to thickness and precursor gas flows," TU delft.

[30] C. Droz, E. Vallat-Sauvain, J. Bailat, L. Feitknecht, J. Meier, and A. Shah, "Relationship between Raman crystallinity and open-circuit voltage in microcrystalline silicon solar cells," *Solar Energy Materials and Solar Cells,* vol. 81, no. 1, pp. 61-71, 2004/01/25/ 2004, doi: https://doi.org/10.1016/j.solmat.2003.07.004.

[31] L. Xiaojiao, Y. JunchuanZ, h. Jiawei, L. Ming, Y. Peizhi, and H. Zhihua, "Boron doped a-SiO$_x$:H prepared by H$_2$ diluted SiH$_4$+CO$_2$ plasma," *International journal of electrochemical science,* vol. 11, pp. 10827-10836, 2016, doi: 10.20964/2016.12.94.

[32] F. R. Jeffrey, G. D. Vernstrom, M. Weber, and K. A. Epstein, "The Effects of Dopant Profiles on the Device Parapmetrs of p-i-n and n-i-p a-Si Solar Cells," *MRS Proceedings,* vol. 70, p. 531, 1986, Art no. 531, doi: 10.1557/PROC-70-531.

[33] A. Richter, V. Smirnov, A. Lambertz, K. Nomoto, K. Welter, and K. Ding, "Versatility of doped nanocrystalline silicon oxide for applications in silicon thin-film and heterojunction solar cells," *Solar Energy Materials and Solar Cells,* vol. 174, pp. 196-201, 2018/01/01/ 2018, doi: https://doi.org/10.1016/j.solmat.2017.08.035.